A Step Towards Imaging Angle Resolved Photoelectrons with X-Ray Radiation for Applications in Gas Phase

Lleah O'Sullivan

A thesis presented for the degree of
Master of Physics

LUNDS UNIVERSITET

Supervisor
Mathieu Gisselbrecht

Division of Synchrotron Radiation
Department of Physics
Lund University
VT 2014

Abstract

Photoionisation dynamics occurring in Ar and N_2O upon the absorption of soft X-ray radiation, have been studied through the extraction of the β parameter from the angular distributions of Ar $2p_{3/2}$ and N_2O N_t 1s photoelectrons by a means of Velocity Map Imaging Spectroscopy.

The results of β determined in the dipole approximation for N_2O at different photon energies, coincided with pre-documented values but this was not so in the case of Argon. The determination of the asymmetry parameter was effected by image distortions and background signal that were present in all of the velocity map images in varying degrees. The photon energy and the energy separation between photoelectron distributions also affected the determination of β.

Possible non-dipole effects in the angular distributions of the N_t 1s state in N_2O were also investigated via the determination of the non dipole asymmetry parameters δ and γ. Unlike β, these parameters could not be determined through inversions of the velocity map images due the symmetry along the spectrometer axis being broken in the non-dipole regime. For an accurate description of the photoionisation process in this instance, such effects should be accounted for, but with the current method it is not possible to observe them.

One aim was to study photoionisation dynamics in gas phase FePc. As a result of inhomogeneous heating of the original solid sample, no data was obtained.

Acknowledgements

I would like to thank my supervisor Mathieu Gisselbrecht. Thank you for your time, knowledge and dedication throughout the duration of my thesis study.

I would also like to express my gratitude to Stacey, Shabnam, Anna, Bart and Erik for providing me with useful resources, much needed programming aid and Tuesday afternoon fika.

I also appreciate the time given to me by Linnea and Per, to help me understand vital components of my thesis work and to those present at the beamtime who were happy to teach me new things.

The time spent working on my thesis was made much more enjoyable by my office companions and fellow physicists. Thank you for the laughs and the physics discussions that have been of great value to me.

This thesis would never have been possible without the constant encouragement from my friends. Thank you for always taking the time to ask me how my writing was going, to listen to me moan and for believing in me when I didn't believe in myself. I cannot express my gratitude enough.

Mum, Dad and Senna, I cannot thank you enough for all you have done for me. Thank you for putting up with me and loving me unconditionally and following me wherever my dreams have taken me. Without you I wouldn't be where I am today, so I owe all of this to you.

Contents

Acronyms

CCD	Charge Coupled Device
DA	Dipole Approximation
EPU	Elliptically Polarising Undulator
FWHM	Full Width at Half Maximum
IP	Ionisation Potential
NEXAFS	Near Edge X-Ray Absorption Fine Structure
PSD	Position Sensitive Detector
UV	Ultra-Violet
VM-Images	Velocity Map images
VMIS	Velocity Map Imaging Spectroscopy
XPS	X-Ray Photoelectron Spectroscopy

Introduction

1.1 Motivation

Kai Siegbahn and workers [1] developed the X-Ray Photoelectron Spectroscopy (XPS) technique as it is known today, and were the first to produce high-resolution XPS spectra from which atomic core level binding energies could be determined. One attribute of XPS is that it demonstrates extreme sensitivity in regards to a systems chemical environment – as is evident by chemical shifts [2] – and thus has found use in a number of applications [3].

In general, the inner shell ionisation of electrons in atoms, molecules and condensed matter, shed light onto important quantities such as ionisation potentials, electron affinities and ionisation cross sections, as well as providing information on the dynamics of the photoionisation process [4].

Recent studies [5] of the ionisation of core level electrons from molecules in gas phase, observed that the stoichiometric ratios of the peaks in the measured XPS spectra were not as expected. It was speculated that the cause was due the intermolecular, elastic scattering processes of outgoing photoelectrons, but such mechanisms had not been considered as being strong influencing factors on the photoionisation process due to the very small size of the molecules used in the study.

Such a finding has prominent effects on the use of inner-shell spectroscopy as a quantitative analytical tool, especially as the interpretation of the spectra does not necessarily give insight into the full dynamics of a photoprocess. The full dynamical information needs to be obtained if all the intrinsic processes that occur upon photoionisation of core electrons is to be understood. Not having access to such information thus has great consequences on the interpretation of photoelectron spectra, especially on those belonging to complex molecules adsorbed on surfaces.

In order to gain a better insight into photoionisation dynamics, it is the aim of this study to measure the angular distribution of photoelectrons emitted from the core levels of atoms and molecules in gas phase. Measuring the angular distribution is a direct measure of the differential cross section; this

can give information on the initial and final states of the target atom or molecule, and can provide the dynamical information of the photoemission process [6]. It is hoped that this can be achieved using a combination of Velocity Map Imaging Spectroscopy (VMIS) and XPS.

Velocity Map Imaging Spectroscopy is predominately a laser based technique that has advanced the measurement of angular distributions and has become indispensable in the field of molecular reaction dynamics [7]. Currently the power of an XPS spectrometer is limited by the amount of information that can be gathered in its small, solid angle of detection, but a VMI spectrometer utilises an electrostatic lens to project the velocity distribution of photofragments over a 4π solid angle onto an imaging detector. Combing the XPS and VMIS techniques would be a novel way to image the full dynamical processes occurring inside molecules following the ionisation of core electrons by X-rays.

The ultimate goal would be to apply this approach to complex systems in gas phase such as metal phthalocyanines, which have important applications in, but are not subjected to, medicine [8], solar cells [9], thin- films devices [10] and gas sensors [11].

1.2 Background

The work was carried out at the MAX-Lab synchrotron light facility. It provides soft X-ray radiation up to the keV range, making it possible to carry out XPS studies on inner shell electrons on which to obtain the angular distributions of photoelectrons emitted as a product of photoionisation. The advantage of using a synchrotron source is that the photon energy can be scanned over a desired range, which allows numerous interaction effects between radiation and matter, for specific orbitals within an atom or molecule, to be studied.

Under the experimental conditions provided at this facility, it has been assumed that the photoprocesses investigated are one photon-one electron mechanisms that occur within the dipole approximation, and that interaction between the soft X-rays and the matter is treated as a perturbation to the Hamiltonian of the electron in the central potential of the nucleus in the weak field case.

A full description of how radiation interacts with matter is both complex and lengthy and it is not possible to explain it in full detail within this thesis. However for this investigation it is imperative that the interaction of soft X-rays with atoms and molecules within the dipole approximation is understood. This section therefore provides a summary of the theory behind

light-matter interaction that is most relevant to this study.

1.2.1 Light-Matter Interaction

The interaction between an electromagnetic field and an electron ($\mathbf{H'}(t)$) can be described as a perturbation of the Hamiltonian of the electron in the central potential of the nucleus ($\mathbf{H}_0$), such that the system at time t can be described by

$$\mathbf{H}_t = \mathbf{H}_0 + \mathbf{H'}(t) \tag{1.1}$$

This perturbation can take form either as a scattering or an absorption event. In the case of absorption of a photon by an atom or molecule, an instantaneous transition of an electron from a low-lying energy state to a higher lying-energy state is induced. This act of photoabsorption, for any given case, has a probability of occurrence given by the photoabsorption cross section

$$\sigma_a = \frac{W_{fi}}{F_{ph}} \tag{1.2}$$

where W_{fi} is the probability of absorbing a photon per unit time per atom, and F_{ph} is the incident photon flux [12]. The quantum mechanical treatment of photoabsorption is described by first order time-dependent perturbation theory and in accordance with this, W_{fi} is described by Fermi's golden rule [12] leading to the general formula for the photoabsorption cross-section for linearly polarised radiation as follows

$$\sigma_a(\omega) = \frac{4\pi^2\alpha\hbar^2}{m^2\omega_{fi}} |M_{fi}(\omega_{fi})|^2 \delta(\omega - \omega_{fi}) \tag{1.3}$$

where α is the fine structure constant, ω_{fi} is the angular frequency of the incident photons, $\delta(\omega - \omega_{fi})$ is the delta function expressing the distribution in ω for a spectral line with zero width, and where $M_{fi}(\omega_{fi}) = \langle f|H'(t)|i\rangle$ is the transition matrix of the perturbation between an initial $|i\rangle$ and final $|f\rangle$ state. As can be seen, the absorption cross-section is directly proportional to the square of this matrix.

As photoabsorption is dominant in the soft X-ray region [13], the intersection of X-rays with atoms or molecules can result in numerous processes transpiring, each with its own probability of occurrence; these can include ionisation, fluorescence and dissociation to name a few. The summation of the eventualities of each possible outcome, is equal to the probability of absorption and thus gives the total photoabsorption cross section, σ_{total}, as

$$\sigma_{total} = \sigma_a = \sigma_{ionisation} + \sigma_{fluorescence} + ...$$

1.2.2 Experimental Manifestation

Two processes in particular that can occur upon absorption of soft X-ray photons are photoexcitation and photoionisation. For the sake of simplicity the absorption spectra of the He atom is shown in Figure 1.1 as the features contained within it give direct evidence of the two processes occurring upon absorption of a photon.

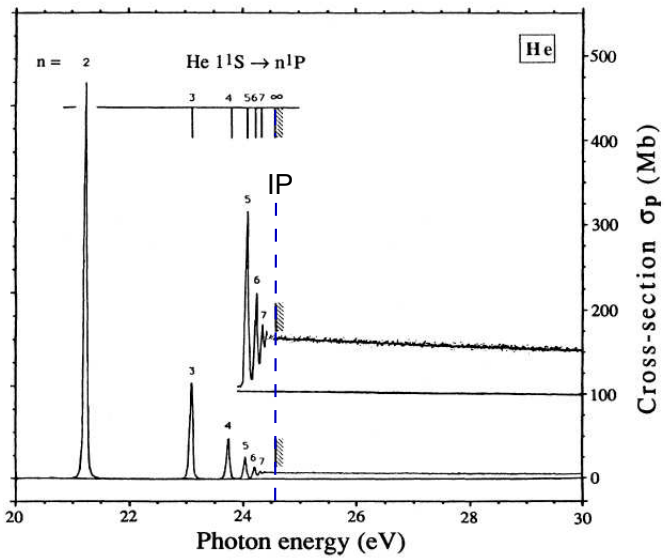

Figure 1.1: The absorption spectra of the He atom obtained by Chan *et al.*(1991) modified from reference [14]. The blue, dashed line indicates the position of the 1s shell ionisation potential.

Photoexcitation

The peaks formed at energies below the blue, dashed line in the spectra are a direct consequence of photoexcitation. This photoprocess occurs as a result of the incident X-ray photon not being sufficient to overcome the ionisation potential (IP) of the target atom. Upon absorption of this photon, a bound valence electron will make an instantaneous transition to another bound but higher lying, unoccupied energy state. The levels which they are promoted to depends on the energy of the incoming photon and dictates the position of the corresponding peak, below the ionisation threshold, within the absorption spectra. Resonant transitions occur if the energy of the photon matches exactly the energy difference between the initial and final unoccupied state

[13]. Equation 1.4 shows the mechanism of photoexcitation of core electrons after the absorption of X-ray radiation,

$$X + h\nu \longrightarrow X^*(1s^{-1}) \tag{1.4}$$

where X^* represents the atom (or a molecule) in an excited state.

Photoionisation

The featureless region in the spectra to the right of the blue, dashed line is indicative of photoionisation. This process occurs when the incident photon energy is sufficient enough to overcome the IP of an atom, thus causing an electron to be ejected from its core, bound state into an unoccupied state in the continuum above the IP [15]. This consequently creates a positively charged ion in a one-hole final state (X^+).

The ejected electron (e^-) is a photoelectron and has a kinetic energy that is related to incident photon energy (hν) and the ionisation potential [16] by

$$E_{kinetic} = h\nu - IP \tag{1.5}$$

Equation 1.6 shows the photoionisation process that occurs after the absorption of X-ray radiation by a target atom or molecule (X).

$$X + h\nu \longrightarrow X^+(1s^{-1}) + e^- \tag{1.6}$$

1.2.3 Dynamics of Photoionisation

The photoelectrons that enter into the continuum are projected in directions that are dependent on the orbital from which they were ejected and the orientation of that orbital with respect to the polarisation vector, $\hat{\mathbf{E}}$, and the propagation vector, $\mathbf{k}$, of the incident radiation [17].

Assuming that the ejected photoelectron is non-relativistic and that its wave vector in the final state ($\mathbf{k}_f$) upon interaction with a plane wave, is related to its final state kinetic energy by $E_f = \frac{\hbar^2 k_f^2}{2m}$, the photoionisation total cross section can be obtained by the integration of equation 1.3 over E_f for all of the final states of the photoelectron. The distribution in angle - relative to an experimentally specified direction - of the intensity of these electrons, is measured by taking the differential of the photoionisation cross section divided by the solid angle $d\Omega = sin\theta d\theta d\phi$, where θ and ϕ are the polar angles of the outgoing photoelectrons wave vector.

This results in the expression for the differential cross section for photoionisation of a single electron, ejected within the solid angle dΩ in the

direction (θ, ϕ), by a photon with a frequency equal to ω [12] being given by

$$\frac{d\sigma}{d\Omega} = \frac{4\pi^2 \alpha \hbar}{m}\left(\frac{k_f}{m}\right)|M_{fi}(\omega)|^2 \tag{1.7}$$

In the case of the interaction of radiation with multi-electron targets, the transtion matrix, M_{fi}, for photon induced transitions between an initial (ψ_i) and final state (ψ_f) becomes

$$M_{fi} = \sum_{\nu=1}^{N} |\langle\psi_f| \exp(i\mathbf{k}.\mathbf{r}_\nu)\hat{\mathbf{E}}.\mathbf{p}_\nu|\psi_i\rangle|^2 \tag{1.8}$$

where $\mathbf{r}_\nu$ and $\mathbf{p}_\nu$ are the position and the momentum operators of a given photoelectron, ν; the sum in ν extends over all N electrons in the system [18] [19] [12]. From this relationship it clear that the differential cross section is highly dependent on $\hat{\mathbf{E}}$, which implies that the direction and the degree of linear polarisation of the radiation is important [19]. A resonant transition between an initial and final state as given by the matrix component of equation 1.7, is most likely to occur when the transition dipole moment is aligned with $\hat{\mathbf{E}}$ [20].

The Taylor expansion of the $\exp(i\mathbf{k}.\mathbf{r})$ element of the transition matrix in equation 1.8 gives

$$\exp(i\mathbf{k}.\mathbf{r}) \approx 1 + i\mathbf{k}.\mathbf{r} + ... \tag{1.9}$$

In the electric dipole approximation (DA) i.e. under the assumption that the wavelength of the incoming radiation is much greater than the Bohr radius of the target [6], only the zeroth order term (the electric dipole matrix element) in this expansion is preserved, resulting in $\exp(i\mathbf{k}.\mathbf{r}) \approx 1$. The higher order terms corresponding to higher order electric quadrupole and magnetic dipole interactions are neglected because they are usually a lot smaller then the zeroth term [18]. In the soft X-ray region this approximation is satisfied and hence is assumed to be valid.

1.2.4 Angular Distribution

In the dipole approximation, photoelectrons that are emitted from randomly oriented targets as a result of one-photon dissociation by linearly polarised light, have a differential cross section and therefore angular distribution [4] [21] [19] [6] given by

$$\frac{d\sigma}{d\Omega} = \frac{\sigma_{total}}{4\pi}[1 + \beta P_2(cos\theta)] \tag{1.10}$$

Here, σ_{total} is the total photoionisation cross section that determines the overall intensity of the process, $P_2(cos\theta) = \frac{1}{2}(3\cos^2\theta - 1)$ with θ being the angle between the polarisation vector of the radiation and the velocity vector of the ejected electron, and β is the characteristic dipole asymmetry parameter that contains all the dynamical information of the photoionisation process.

Four possible angular distributions of the emitted photoelectrons, as a function of angle and with respect to the polarisation vector, are shown in figure 1.2. The distributions overlap at the magic angle of 54.7^o. At this angle the angular distributions of emitted photoelectrons can be measured independent of the β value. Measuring over all angles, as is this case in this work, allows the dependency of the differential cross section on the asymmetry parameter to be elucidated.

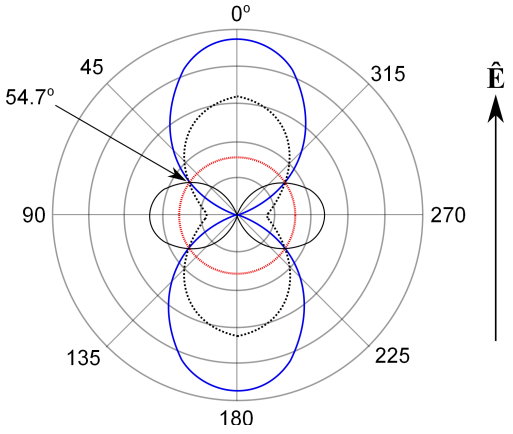

Figure 1.2: Polar plots of the photoelectron differential cross sections. Blue line: $\beta = 2$ indicating preferential emittance in the direction of the polarisation vector. Black dashed line: $\beta = 1$. Red line: $\beta = 0$. Black line: β= -1 indicating preferential emittance perpendicular to the direction of the polarisation vector. Arrow at 54.7^o indicates the magic angle where the cross sections are the same independent of β.

1.2.5 The β Parameter

The β parameter - also known as the asymmetry parameter - depends on, the dipole radial matrix elements ($\sigma_{l\pm1}$) and the interference of the lth partial waves of the photoelectrons in the continuum (δ_l), as shown by equation 1.11.

$$\beta = \frac{l(l-1){\sigma_{l-1}}^2 + (l+1)(l+2){\sigma_{l+1}}^2 - 6l(l+1)\sigma_{l+1}\sigma_{l-1}\cos(\delta_{l+1} - \delta_{l-1})}{3(2l+1)[l{\sigma_{l-1}}^2 + (l+1){\sigma_{l+1}}^2]} \tag{1.11}$$

where l is a state given by *s, p, d..* and so on [4]. The β parameter can range from a value of +2, which reveals that photoelectrons will be ejected preferentially in the direction of the polarisation vector of the incoming radiation, to a value of -1 which reveals a preference for sideways emission of the ejected photoelectrons with respect to the polarisation vector [6][22] (refer to figure 1.2).

In the central potential model approximation, single photon ionisation from a closed, s subshell of an atom gives only one possible final state channel of the transition matrix [6]. Due to the conservation of angular momentum, this corresponds to a $ns \rightarrow \varepsilon p$ transition where εp is the state of the electron in the continuum, which along with the final state of the atom (ϕ_f) dictates the overall final state i.e. $|\psi_f\rangle = |\phi_f \varepsilon p\rangle$ [23].

Thus from equation 1.11, the angular distribution of the photoelectrons ejected from s shells shows a $\cos^2\theta$ behaviour for all photon energies giving β=2 [4]. However, studies have shown that in atoms other than Helium the asymmetry parameter, upon photoionisation of s shells, can take on alternative values from this energy-independent, predicted value [6].

Houlgate *et al.*(1976) [24] determined the value of the asymmetry parameter over a range of energies just above threshold for the outer 3p shell of the Argon atom. The value of β varied as a function of photon energy and was best emulated by theoretical models which took into consideration intrachannel interactions. See figure 1.3.

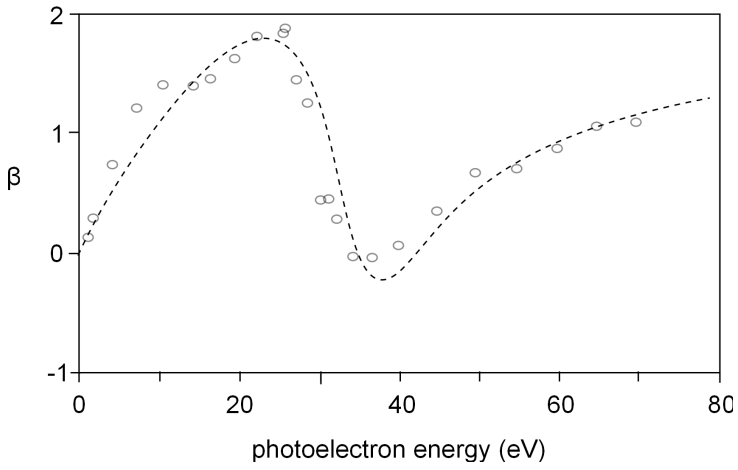

Figure 1.3: Sketch of the dependence of β on the photon energy near threshold for the 3p Argon shell as measured by Houlgate *et al.* [24]. Circles represent the experimentally measured values and the black dotted line represents the RPAE theoretical model, that includes interchannel interactions.

This considerable form of variation of β was explained as the intrachannel interaction being caused by the interference affect between the two competing ionisation channels, εs and εd (photoionisation of non s shell electrons, results in there being more than just one final state channel for photoelectron escape). The relative phase and magnitudes of the two waves as a function of energy influences β through equation 1.11 and ultimately decides the form of the angular distribution. Thus the study of the angular distribution provides all the information on the photoionisation dynamics [25], whilst elucidating the static information on the initial and final states of the target [6].

1.3 This Work

In this work, VMIS and XPS have been combined and used to investigate the full photodynamics of atomic Argon (Ar) and molecular di-Nitrogen Oxide (N_2O), that occur upon inner shell photoionisation with soft X-ray radiation.

The knowledge obtained using this technique about the photodynamics that materialise in these simpler systems is then intended to be applied to studies on gas phase Iron phthalocyanine (FePc), so that the processes that transpire within this molecule upon photoionisation of its inner shells, can be revealed and possibly used to understand if characteristic features observed in the spectra of studies conducted previously, are intrinsic to the molecule or dependent on its environment i.e if its adsorbed on a surface.

These studies were carried out at the MAX-Lab synchrotron light facility over two, one week periods upon installation of the VMI spectrometer to the end of the beam line. Argon was studied using energies close to the threshold of the $2p_{3/2}$, state as at energies just above and below it, interesting photoprocesses have been observed and it would be intriguing to see if the imaging XPS technique could successfully resolve these phenomena. The N_2O molecule was also studied at low energies for the same reason.

The raw VM-images created upon detection of photoelectrons by the VMI spectrometer, were corrected, iteratively inverted and energy calibrated using a partially developed Matlab code. The inverted images were then further analysed so that the asymmetry parameter, β, could be recovered from the angular distributions of the photoelectrons from the inversions. The β values obtained for both Ar and N_2O were compared to previously determined values, and used to interpret the photoprocesses occurring within these systems and to determine the efficiency and reliability of the imaging XPS technique.

To study FePc, an oven was specially designed and implemented during the beam time in order to sublime the molecule.

Methods

The experiments were conducted on the I1011 beamline at the national synchrotron light facility MAX-Lab, located in Lund, Sweden. This beamline is predominantly dedicated to the study of surface science but for the first time during these investigations, it was used for gas phase studies. The NEXAFS spectra required for energy calibration and sample identification are also obtainable at I1011. The photoelectrons were detected and analysed by a VMI spectrometer provided by the Atomic physics department at Lund University.

This section includes details on the XPS and NEXAFS techniques used to acquire the data of interest, details on the MAX-Lab facility and VMI spectrometer set-up, as these were the specialised tools used to carry out the investigation and relevant calibration information. Also in this section is a description of the program used to analyse the raw data files and to extract the relevant photodynamical information from the velocity map images (VM-images).

2.1 Experimental Methods

2.1.1 Inner Shell Spectroscopy

Soft X-ray radiation is useful not only for the study of valence electrons, but for the study of core electrons also. Figure 2.1 shows the mechanics of both photoexcitation and photoionisation in this case.

Two inner shell spectroscopy techniques that are based upon these principles are X-Ray Photoelectron Spectroscopy - which utilises photoionisation - and Near Edge X-ray Absorption Spectroscopy (NEXAFS) - which utilises photoexcitation. They are used in conjunction with one another as XPS gives information about occupied electronic states and NEXAFS gives information on unoccupied bound, or continuum states [26], thus providing a complete picture of the orbital structure of a sample under investigation.

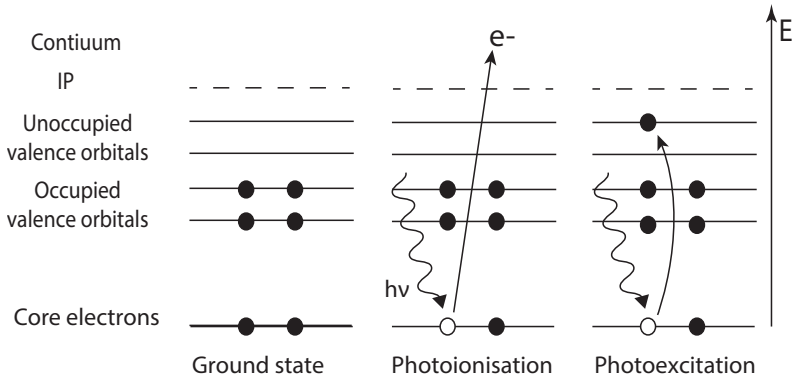

Figure 2.1: Schematic diagram of core orbital photoionisation and core orbital photoexcitation. The open circles represent the 'holes' left in the core orbital due to the ejection of an electron.

XPS

XPS is based on the principle of the photoelectric effect [27] and uses X-ray radiation to induce the photoionisation of core electrons from an atom or molecule. From the kinetic energies of the ejected photoelectrons it is possible to obtain the ionisation potential of a core level according to equation 1.5. The IP of an orbital is element specific and therefore, the set of peaks shown in an XPS spectra are characteristic of that element.

As well as providing elemental details, XPS can provide some chemical bonding information, as shifts in the energies of ionisation potentials caused by chemical bonding (chemicals shifts), can be used to identify chemical compounds and molecules. Extensive investigations on core level binding energies and their shifts due to chemical bonding have been carried out by Kai Sieghbahn and co-workers [16].

NEXAFS

Near Edge X-ray Absorption Spectroscopy is the measurement of the photon absorption features, close to the ionisation edge, created when core-shell electrons make a transition to unoccupied orbitals. In NEXAFS, the energy of X-ray radiation is varied across the ionisation edge of an atomic orbital. The energy levels of the orbitals that the photoexcited electrons occupy, give rise to the distinct peaks in the a NEXAFS absorption spectra. Varying the photon energy allows transitions of electrons to different unoccupied orbitals and therefore different peaks to be investigated [28].

NEXAFS is most useful as a technique for chemical analysis, as atoms and molecules can be identified by the peaks in the absorption spectra; This is

advantageous for energy calibration measurements and for certification of an atom or molecule under study. Furthermore it can also be used to determine the composition and orientation of molecules on substrates. [28]

2.1.2 Synchrotron Radiation Facility

The MAX-Lab synchrotron light facility consists of an injector, three storage rings (MAX I, MAX II and MAX III), beamlines and experimental chambers. Like any other synchrotron facility, it makes use of the fact that charged particles travelling along circular paths are subject to the Lorentz force and as a result of the corresponding centripetal acceleration, they will emit electromagnetic radiation. In the limit of relativistic velocities, the electrons emit electromagnetic radiation with a cone shape emission pattern in a pronounced forward direction [29]. At this facility electrons are created by an electron gun, accelerated by a linear accelerator and depending on their energy are propelled into either MAX I, MAX II or MAX III.

The Storage Ring: MAX II

The electrons enter MAX II with a maximum energy of 400 MeV. They are then further accelerated by radio-frequency cavities to an energy of 1.5 GeV, resulting in this ring being optimised to produce radiation in the ultraviolet, soft X-ray and hard X-ray range.

MAX II is a third generation synchrotron source and uses only insertion devices - mainly undulators placed along the straight sections of the storage ring, along the path of the electron beam - to maximise the production and to optimise the characteristics of the electromagnetic radiation it creates. They are comprised of a periodic series of magnets that alternate in polarity, which increase the intensity of the emitted radiation as a result of interference effects [26].

There are two types of undulator on the storage ring that generate the radiation. The first type is a planar undulator; this produces radiation which is horizontally polarised. The second type, used on the I1011 beamline, is an Elliptically Polarising Undulator (EPU) which was set to provide linearly polarised radiation during this study, as it is a requirement of the VMI spectrometer.

The Beamline: I1011

The I1011 beamline provides soft X-ray radiation in the energy range between 200 eV to 2 keV and contains numerous components that optimise the spectral characteristics and geometry of the synchrotron radiation.

The I1011 beamline is based on a collimated grating monochromator design that allows scanning of the radiation over a particular energy range. The pre-focusing of the soft X-rays from the EPU is achieved with the use of a vertically collimating and horizontally focusing toroidal mirror. The radiation then enters the monochromator which consists of a plane mirror, a 1221 lines/mm plane grating and exit slits. The monochromator is designed to single out a selected wavelength from the distribution of wavelengths of the incoming soft X-rays. The radiation is then focused onto the exit slit by a vertically focusing, cylindrical mirror.

The exit slit is vertical in its orientation and its width - which determines the energy band width of the radiation - the photon energy resolution and the photon flux, can be changed by a computer controlled stepper motor. The radiation passes into the interaction region of the VMI spectrometer upon exiting the monochromator.

Beamline Calibration

The NEXAFS spectra of Argon has been obtained in order to determine the energy of the photon beam and the resolving power of the set up. Absorption measurements of the 2p Argon edge in the soft X-ray regime have been documented in past works [30] [31] which makes it an ideal reference source.

To calibrate the energy of the soft X-ray beam, the photon energy was scanned between 243-252 eV close to the Argon L-edge when the exit slit width was set to 500μm. The measured absorption data is shown in figure 2.2 by the black, finely dashed line.

Peak 1, according to [31], corresponds to the $2p_{3/2} \longrightarrow 4s$ resonant transition and therefore should be centred at a photon energy of 244.39 eV [32]. The energy scale has been calibrated in relation to this, verifying an energy difference of +0.6 eV between the measured and the actual incident photon energy. Thus the other peaks in the spectra have been associated with transitions to unoccupied Rydberg orbitals, corresponding either to $2p \longrightarrow ns$ $(n \geq 4)$ or $2p \longrightarrow nd$ $(n \geq 3)$ transitions. The assignment of each is shown in the table of figure 2.2

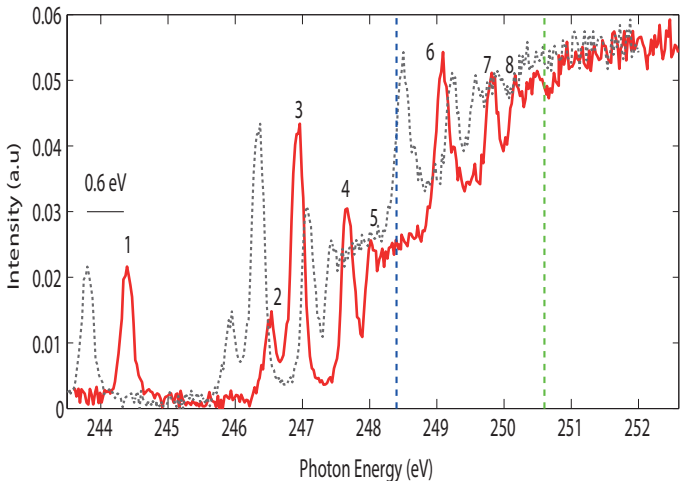

Peak Number	Transition
1	$2p_{3/2} \rightarrow 4s$
2	$2p_{1/2} \rightarrow 4s$
3	$2p_{3/2} \rightarrow 3d$
4	$2p_{3/2} \rightarrow 4d$
5	$2p_{3/2} \rightarrow 5d$
6	$2p_{1/2} \rightarrow 3d$
7	$2p_{1/2} \rightarrow 4d$
8	$2p_{1/2} \rightarrow 5d$

Figure 2.2: The Measured Argon L-edge NEXAFS spectra is represented with the corresponding peak assignments according to references [31] and [32]. Red line: Energy calibrated data. Black finely dashed line: Original measured data. Blue dashed line: Threshold of $2p_{1/2}$. Green dashed line: Threshold $2p_{3/2}$

The $2p_{3/2} \longrightarrow 4s$ peak in figure 2.2 is isolated from other features in the spectrum and, unlike the other peaks, is not obviously affected by the nature of the background signal. As a result, a Voigt profile has been fitted to these data points using a least-square residual fit to determine the resolving power of the set up (see figure 2.3). The Voigt profile is a convolution of the Lorentzian probability density (which accounts for the homogeneous broadening of the spectral peak, due to the natural lifetime of the state) and the Gaussian probability density (which accounts for the inhomogeneous broadening of the spectral peak, due to imperfections of the monochromator and spectrometer). In this case it has been assumed that Doppler and pressure broadening's are negligible. The fitting of the $2p_{3/2} \rightarrow 4s$ transition gives a Gaussian resolution of 0.15 meV at 244.39 eV, leading to a resolving power of R$\sim$16,350 for this peak according to the relation $R = \frac{E_{peak}}{\Gamma_G}$.

To investigate the effect of the exit slit width on the resolution, the NEXAFS spectra of N_2O were obtained at slit widths of 500μm, 250μm and 125μm. It was found that the photon energy resolution of the spectra increased with decreasing slit width. In opposition to the increased resolution, the amount of noise detected in a spectra also increased. Therefore in selection of the slit size, a compromise must be made between the amount of resolution achievable and the amount of noise that will be present in the spectra.

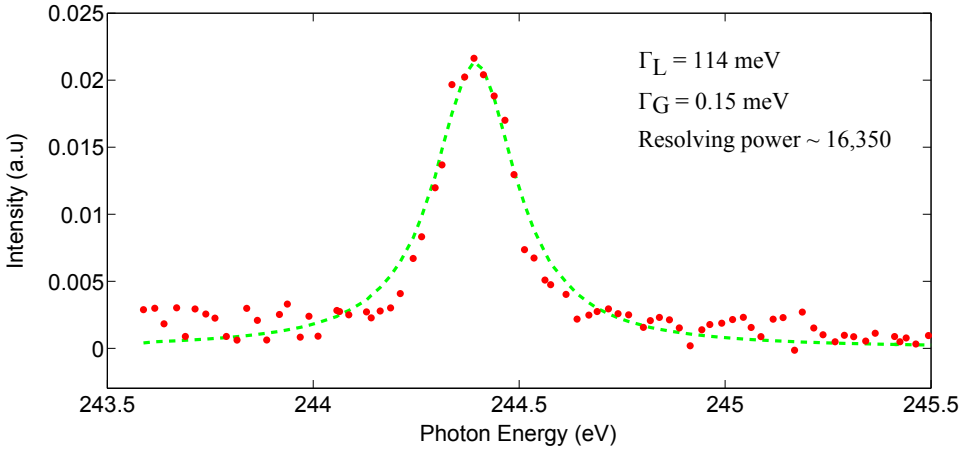

Figure 2.3: The experimental Ar $2p_{3/2} \rightarrow 4s$ data (red dots) with a fitted Voigt profile (green line) from which the Lorentzian (Γ_L) and Gaussian (Γ_G) line widths have been determined.

2.1.3 Velocity Map Imaging Spectrometer

Velocity map imaging is a technique that acquires the 2D projection of a 3D velocity distribution of photofragments created during a photoprocess [33]. The photofragments are detected over a 4π solid angle which means that a full collection efficiency is achieved during detection.

VMI has become a key tool in studies investigating photodissociation and reaction dynamics, scattering and dissociative charge exchange and recombination [34], to name a few. It has also become a central component in imaging photoelectron spectroscopy as its ability to obtain energy and angular distributions measurements simultaneously, for all photoelectrons that are released during a photoprocess, gives it a great advantage over conventional time-of-flight and electrostatic electron energy analysers. The VMI spectrometer is predominantly used in laser based studies and so the implementation of it on a soft X-ray beamline for this investigation is a novelty.

Spectrometer Design and Principle

The velocity map imaging spectrometer used during this investigation had the same design as that of Eppink and Parker [35], such that it utilises an electrostatic immersion lens to focus all particles - with the same initial velocity vector - created within the photoprocess onto the same point on a detector, irrespective of their point of creation within the interaction volume. The electrostatic lens is produced from a simple configuration of three, flat

and annular electrodes and gives an increased image resolution [36] from that obtained by other imaging procedures such as the ion imaging technique developed by Chandler and Houston [37].

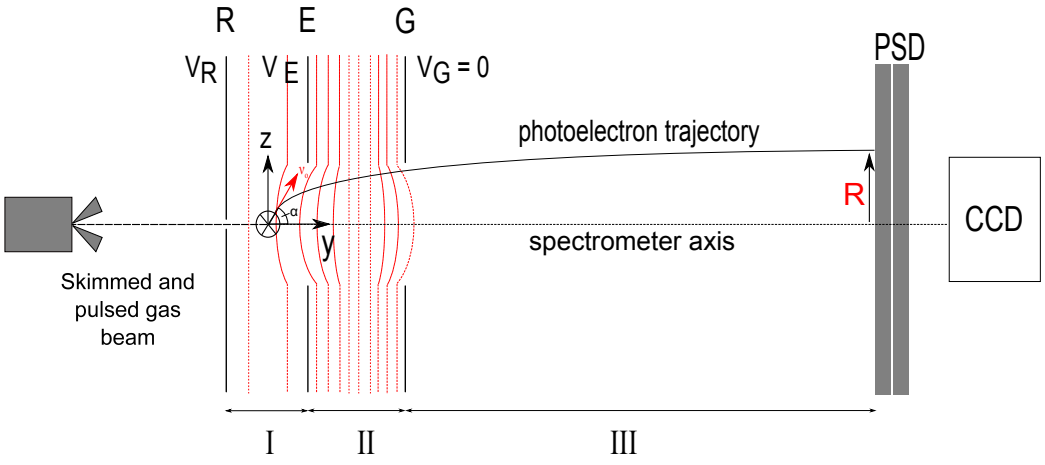

Figure 2.4: Schematic drawing of the VMI spectrometer. The three electrodes are symbolised by R for repellor, E for extractor and G for ground. They are held at voltages of V_R, V_E and $V_G = 0$ respectively. The propagation of the soft X-rays is directed into the page and the interaction volume is symbolised by the circled cross. The electric field lines are portrayed by the dashed red lines with the shape of electrostatic immersion lens, created by the electrode design, clearly depicted in region II. The field in region II is inhomogeneous and can be adjusted by changing the voltage across the electrodes whereas region (III) is devoid of an electric field. At the opposite end from the extraction region is a detection system consisting of a 2D PSD - comprised of a stack of multi-channel plates coupled to a phosphor screen - and a CCD camera. The position where a photoelectron hits the detector is given by R.

The VMI spectrometer has an extraction region (I) and an accelerator region (II) at one end of a time-of-flight tube (III). It was installed directly to the end of the beamline and oriented such that the soft X-ray beam entered the spectrometer through region I and was aligned perpendicular to the time-of-flight tube (spectrometer axis). The beam was vertically polarised with respect to the detector plane to ensure the rotation around the x-axis is invariant.

The gas samples entered the spectrometer via a gas input fixture that was mounted in line with the spectrometer axis, after passing through a skimmer with a 2mm opening. The design of the skimmer optimises the beam geometry and forces the beam to be collimated at the position where it intersects the photon beam; this ensures that the interaction volume (it is a volume and not a point due to the beams having finite widths) is small and defined, resulting in high quality velocity map images. The jet of particles was pulsed through the skimmer to keep the background pressure in the extraction region of the spectrometer low.

The particles within a gas bunch, then passed through a small gap in the repellor electrode and intersected the soft X-ray beam at a 90^o angle in the extraction region. The engagement of the two beams resulted in the emission of photoelectrons, in all directions of space, that were propelled into the accelerator region in response to the voltage applied across the electrodes. The ratio between the voltage of the repellor and extractor electrode, $\frac{V_E}{V_R}$, was optimised such that the lens created in region II, focused and directed identical, charged particles through the time-of-flight tube to the same position on the focal plane of the 2D position sensitive detector (PSD). During the investigation, this ratio was optimised at 0.762 for the detection of photoelectrons. The positions where the photoelectrons were detected on the PSD surface were registered by a charge coupled device (CCD) camera placed behind it.

In order to remove the possible sources of contamination within the chamber that give rise to background signal and prevent the photoelectrons reaching the detector, a pressure of around $1 \times 10^{-7/-8}$mbar was maintained within the system by for-vacuum and turbopumps, mounted at both the detector and main chamber ends of the spectrometer.

2.2 Analysis

The core of the analysis was to extract the value of the β parameter, for the Ar and N_2O samples at different photon energies. This was achieved with the use of a partially developed Matlab program, written by Per Johnsson from the Atomic physics department at Lund university, which contained within it the iterative inversion procedure of Vrakking(2001) [38]; this inverted the VM-images such that a reconstruction of the original 3D velocity distribution of the photoelectrons was produced. It was then possible to determine the β parameter from the inverted image after further analysis.

The Matlab program was originally created for investigations using laser light and had not been intended to be used to find the β parameter. As a consequence, it was not perfectly suited for this work, thus the pre-existing code was modified and new code was developed to account for this. After these modifications, much effort was put into understanding the code and working out how it could be manipulated to produce optimised VM-images. This was done through preliminary work which consisted of investigating the effects of background signal on the correction of the image, finding the optimal amount of background subtraction required for each data file and deciphering the most appropriate symmetry of the final corrected image.

2.2.1 Interpretation of the VM-Images

Upon ionisation of the core levels of the gas particles, photoelectrons are emitted in all directions in space creating a 3D velocity distribution which contains the energy and angular distribution information of the photoprocess [36]. However due to the acceleration they are subjected to within the spectrometer, the 3D distribution is 'crushed' along the spectrometer axis leading to a circular image being formed on the 2D detector where the particles impact on it. This circular image is a velocity map image and ultimately is the 2D projection of the former 3D velocity distribution of the particles created during the photoprocess.

The position where a photofragment collides with the PSD is directly related to its initial velocity ν_0, regardless of its original point of creation in the interaction volume. As a result of the 'crushing', the velocity component parallel to the spectrometer axis is lost, but the transverse component of ν_0 is unaffected.

The position where the photofragments are detected by the detector (R as shown in figure 2.4) is directly related to the transverse component of the velocity by

$$R = \nu t \tag{2.1}$$

where t is the time of flight of the photofragments towards the detector. From the relationship $E_k = \frac{1}{2}m\nu^2$, equation 2.1 can be re-written in terms of kinetic energy such that

$$R = t\sqrt{\frac{2E_k \sin\alpha}{m}} \tag{2.2}$$

where m is the mass of the particle. The position of detection is then directly related to the particles kinetic energy.

Knowing that the position of detection of the photoelectron is directly related to the kinetic energy, and that the kinetic energy is related to the binding energy and the photon energy by equation 1.5, it is then possible to identify which orbital within the atom or molecule the photoelectron was ejected from.

VM-Image Example

Tests were carried out on the spectrometer, in the Atomic laser laboratory at Lund University, to check its performance. High Harmonic Generation from infra-red light was used to ionise Argon and the resulting VM-image and its subsequent inversion are displayed in figure 2.5.

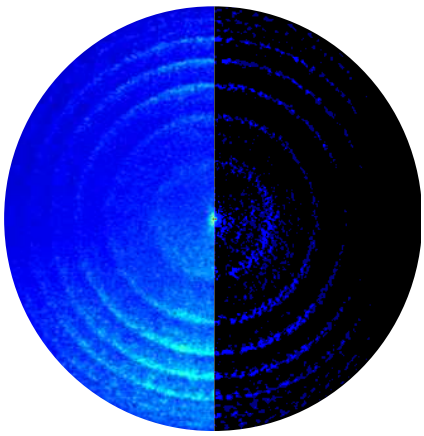

Figure 2.5: Left half:corrected VM-image of atomic Argon when ionised by laser light. Right half: the subsequent inversion

The ground state, electronic configuration of the the Ar atom is $1s^2 2s^2 2p^6$ $3s^2 3p^6$. The five rings that are clearly visible in the VM-image, represent the velocity distributions of the photoelectrons ejected from the 2p shell by five consecutive, odd harmonics - H_{11}, H_{13}, H_{15}, H_{17} and H_{19}. They are well resolved in both the VM-image and the inversion - the details of inversions shall be discussed later. Thus it seems that the spectrometer set-up is fully optimised to produce images with a quality good enough for inversion.

2.2.2 Background Subtraction

Due to the nature of the synchrotron source, background signal was present in every VM-image - in various amounts depending on the photon energy and sample - and was concentrated mainly near the image centre. In order to determine the effect of this signal on the asymmetry of the raw VM-image, a plot of the signal intensity as a function of pixel number was analysed for a defined region in the image where most of the background was located. Varying amounts (determined by a numerical factor) of pure background signal were then subtracted from the raw data until an even and reduced intensity distribution of this signal in the image was achieved. The value of the factor that provided the optimal amount of asymmetry reduction without compromising the intensity of the original data, was applied to the background that was subtracted from the raw image before it underwent further analysis

Table 2.1 shows the factors by which the background was subtracted from each individual file obtained at a given photon energy.

Ar	
Energy (eV)	Background subtraction factor
270.6	1.3
252.6	2.3
251.6	2.6

N_2O	
Energy (eV)	Background subtraction factor
437.6	0.33
430.6	1.3
420.6	1.3

Table 2.1: The values of the background factor applied to each file investigated

2.2.3 Analysis Program

The program used for analysing the collected, raw data consisted of five stages;

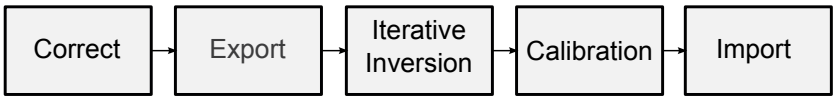

A description of the four relevant procedures for the determination of β are given.

Correct

Once a raw data file is read into the program it is first subjected to the 'correct' action. The main purpose of this action is to determine the image centre and to reduce the ellipticity of the image, as it is a requirement of the inversion procedure that the image be cylindrically symmetric [38]. Smoothing of the image is also applied within this stage of the analysis procedure as the angular distribution (from which β is to be extracted) is strongly dependent on the quality of the inversion and therefore, the accuracy in its measurement is dependent on the angular resolution [7].

The image centre was determined by selecting the x and y pixel coordinates from the Cartesian raw image from which the program could base an estimate of the image centre. Any ellipticity was corrected for by choosing a specific region within the polar representation of the Cartesian image that the program could apply inbuilt corrections to.

These input variables were then set to the values that the pre-written program determined as optimal for the correction of the centre and ellipticity for each background corrected image. These parameters were saved and unchanged throughout the rest of the analysis, so that consequent subtraction of the background would not effect the centre and ellipticity corrections, as it was found from previous testing that this was the case.

Export

Through the export action, the corrected Cartesian VM-image is changed to a format that the executable inversion procedure can understand. Within this action it is also possible to input the number of iterations that the inversion program should carry out. In this work it was chosen that the inversion procedure would perform twenty-five iterations, as with this number, an acceptable level of convergence between the calculated and experimental

distributions can been achieved [7] within a reasonable time. It is also possible to select the final image symmetry, but during this work it was chosen that no symmetry would be applied to the corrected VM-images.

Iterative Inversion

The corrected images are then subjected to the same iterative inversion procedure as developed by Vrakking [38]. This method is based on the realisation that there exist similarities between the angular and radial distributions in the 3D and 2D data.

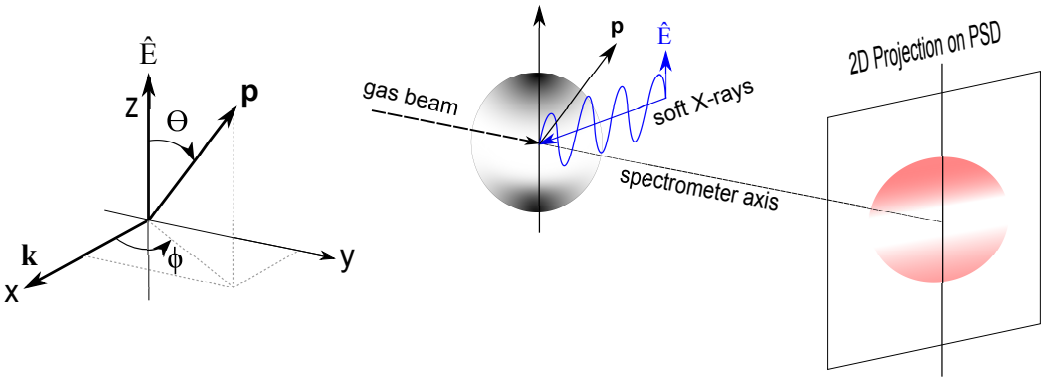

Figure 2.6: Left: The coordinate system of the VMI set up. The vectors $\hat{\mathbf{E}}$, $\mathbf{k}$ and $\mathbf{p}$ indicate the directions of the linear polarisation, photon propagation and the photoelectron momentum respectively. The angle between the z-axis and $\mathbf{p}$ is denoted by θ. Right: Schematic view of the 3D velocity distribution of photoelectrons after photoionisation (grey sphere) and the resulting 2D projection after it has been 'crushed' along the spectrometer axis (red circle).

Using the fact that the 3D velocity distribution, P(x,y,z), is cylindrically symmetric around a symmetry axis in the experiment, it can be written as the product of a radial distribution, $P_1(r)$, and a radial-dependent angular distribution ($P_2(r,\theta)$) as shown in equation 2.3.

$$P(x,y,z) = P(r,\theta,\phi) = P_1(r)^* P_2(r,\theta) \tag{2.3}$$

The 2D distribution is captured in the z-x image plane of the PSD. The angle between the z-axis and the photoelectron momemtum vector $\mathbf{p}$ is depicted by θ. Conventionally θ takes values from 0 to π in the case of x > 0. The 3D velocity distribution is normalised to give

$$2\pi \int\int P_1(r) r^2 P_2(r,\theta) sin\theta d\theta dr = 1 \tag{2.4}$$

where 2π indicates the integration over the full theta range. Additionally, the 2D experimental distribution can also be written as a product of a radial distribution, $Q_{1,exp}(r)$, and a radially dependent angular distribution $Q_{1,exp}(r,\alpha)$, in the form

$$Q_{exp}(x,y) = Q_{exp}(r,\alpha) = Q_{1,exp}(r)^* Q_{2,exp}(r,\alpha) \tag{2.5}$$

where normalisation of the 2D image gives the condition

$$\int\int Q_{1,exp}(r) r Q_{2,exp}(r,\alpha) d\alpha dr = 1 \tag{2.6}$$

where α is the 2D representation of θ and has values from 0 to π in the case of x $>$ 0 and values from π to 2π for x $<$ 0.

Working with the normalised angular distributions and using the convention of the values of α as described, the experimentally observed 2D radial and angular distributions ($Q_{1,exp}(r)$ and $Q_{2,exp}(r,\alpha)$) can be used to derive the first estimates of the 3D radial and angular distributions ($P_1(r)$ and $P_2(r,\theta)$) thus giving the ansatz

$$P_{1,i=0}(r) = Q_{1,exp}(r)/2\pi(r) \tag{2.7}$$

$$P_{2,i=0}(r,\theta) = Q_{2,exp}(r,\alpha=\sigma) \tag{2.8}$$

where i denotes the iteration index. From these relations, a new 2D image is calculated resulting in a new 2D radial and angular distribution being acquired in the form

$$Q_{1,i=0}(r)^* Q_{2,i=0}(r,\alpha) \tag{2.9}$$

The experimental 2D distribution from equation 2.5 is iteratively compared to the calculated 2D distribution from equation 2.9 until they coincide with each other within a reasonable limit. The corrections are then applied to the 3D velocity distribution conferring to

$$P_{1,i}(r) = P_{1,i-1}(r) - c_1[Q_{1,i-1}(r) - Q_{1,exp}(r)]/2\pi r)$$

$$P_{2,i}(r,\theta) = P_{2,i-1}(r,\theta) - c_2[Q_{2,i-1}(r,\alpha=\theta) - Q_{2,exp}(r,\alpha=\theta)]$$

The parameters c_1 and c_2 determine the size of the corrections to be applied.

The result of the iterative inversion is that the 3D velocity distribution of the photofragments has been reconstructed from the 2D projection that is detected experimentally.

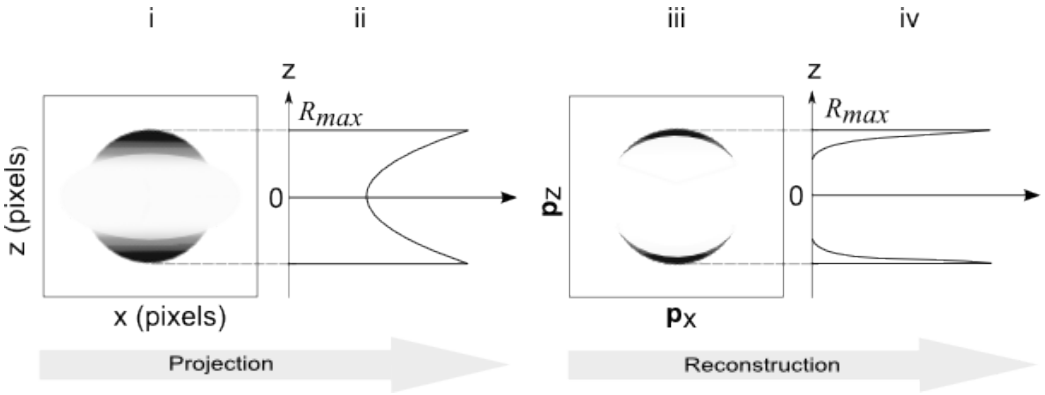

Figure 2.7: A 3D velocity distribution projected onto a 2D plane results in a blurred ring in the VMI image (i). After the inversion of the 2D projection, the original sharp 3D distribution is retrieved, but in a 2D image only a 2D section of it is displayed (iii). The slices through these images along the polarisation axis (z) are shown by (ii) and (iv).

The main advantage of the iterative procedure is that unlike other inversion methods, the noise in the inversion is projected towards the centre of the image, where it usually doesn't interfere with relevant features within the image [38].

Calibration

Both the inversion images of N_2O and Ar contain rings that can be energy calibrated within this action. For any given photon energy, the kinetic energy of the electrons is known (from equation 1.5) thus the rings can be calibrated and separated according to their kinetic energies.

Results and Discussions

3.1 Photoionisation Dynamics in Atomic Ar

Angle resolved photoemission studies of the outer shells in Ar have been conducted experimentally and theories have been developed that complement the results. For instance, Houlgate *et al.* (1976) [24] determined the values of the asymmetry parameters for 3p Ar electrons in the energy range from 0-70 eV above threshold, using a synchrotron light source. The trend of β as a function of photon energy was best emulated by theoretical models that took into consideration intrashell exchange interactions i.e. interactions between the outgoing and remaining electrons.

Lindle *et al.*(1988) [39] studied the ionisation of the 2p inner shells of Ar under the assumption that the same theoretical models that accurately described the variation in the asymmetry parameter for the outer shell of Argon would do so in this case, but it did not. What is surprising is that the variation in β for the 2p shell of Neon is accurately described by the valence shell model, which then supports the idea that it should successfully describe the asymmetry parameter of the Ar 2p shell.

It is then of interest to investigate the full dynamical processes occurring in the Ar 2p shell using the imaging XPS technique. This was achieved by obtaining the β values from the angular distributions of photoelectrons from the Ar $2p_{3/2}$ state, at photon energies of 270.6 eV, 252.6 eV and 251.6 eV; The two lowest energies are near threshold energies. The results of the asymmetry parameter, a discussion of how they were obtained and the dependability of the analysis will be presented in this section.

The optimised VM-images obtained at these photon energies, as well as their respective inversions are shown in figure 3.1.

Ionisation of the inner 2p subshell results in the ejection of core electrons from the two fine structure states, $2p_{1/2}$ and $2p_{3/2}$, providing that the photon energy is high enough to overcome the ionising potential of each state, which are 250.6 eV and 248.4 eV respectively [39]. As the IP of the $2p_{3/2}$ is lower than that of the $2p_{1/2}$, the photoelectrons, according to equation 1.5, will

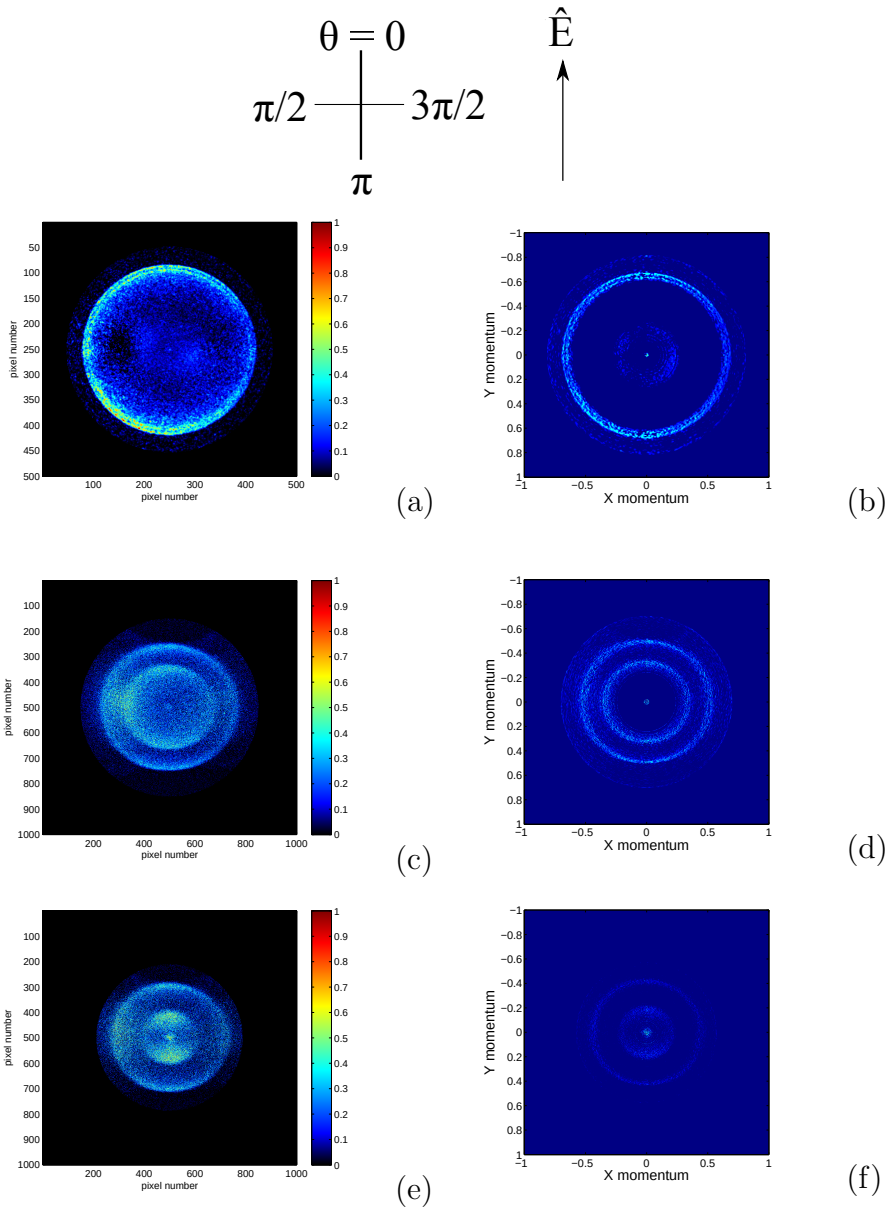

Figure 3.1: The optimised VM-images obtained from the Ar 2p shell at a) 270.6 eV b) 252.6 eV and c) 251.6 eV with images b), d) and f) being their respective inversion. The angle within the images is shown by the axis, the direction of the polarisation vector with respect to all the images is given by the vertical arrow above the images.

be released with a greater kinetic energy. As the radius is proportional to this energy, as shown in equation 2.2, the largest ring in the VM-image will correspond to electrons ejected from this state.

Comparing the three VM-images, it is clear to see that the intensity of the detected photoelectrons decreases with decreasing photon energy but the amount of noise in the image becomes more prominent. Figures 3.1c and 3.1e, even with background signal removed, are still affected by signal which interferes with the important features. This is most problematic in figure 3.1e as the noise overlaps the outer $2p_{3/2}$ ring at $\theta = \pi/2$ and is subsequently passed through into the inversion from which β will be determined. The main cause of this unwanted background signal is most likely due to scattering effects within the experimental chamber, for instance from the production of secondary electrons upon collisions between Auger electrons and the chamber walls.

At a photon energy of 270.6 eV, the photoelectrons are released from the $2p_{1/2}$ and the $2p_{3/2}$ states with kinetic energies equal to 20 eV and 22.2 eV respectively (refer to equation 1.5). The two rings representing these distributions are most resolved at values of theta closest to zero degrees in the VM-image, but blurring of the distributions does occur at the other angles. This blurring is carried through into the inversion which makes the two distributions difficult to separate but again, at angles closest to zero degrees, there are clearly two distinct energy regions.

In order to determine β, the Cartesian inversions were converted to polar coordinates such that the distributions of the photoelectrons were depicted as a function of their kinetic energy with respect to the detection angle. The resulting polar images are shown in figure 3.2.

In an optimised VM-image, the rings in the inverted images should be represented by horizontal straight lines in the polar images, as at all angles, the kinetic energy of identical photoelectrons should be the same. It appears however, that the lines are suffering from slight distortions, especially in the outer stripe and mainly in images 3.2c and 3.2e where the energies are close to threshold. This image distortion is most likely due to skewing in the z=x axis of the detector plane and it manifests itself in the form of 'wiggles' in the horizontal stripes. The distortion in the inverted image most likely originates from distortions in the raw image caused by residual aberrations of the spectrometer electrostatic lens [7].

The line at the highest photoelectron energy in the polar image, corresponding to the $2p_{3/2}$ photoelectrons, was selected for the determination of β. This was done through the appropriate selecting of a minimum and maximum kinetic energy from a plot of the image intensity against photoelectron energy. These such plots are displayed in figures 3.2b, d, and f.

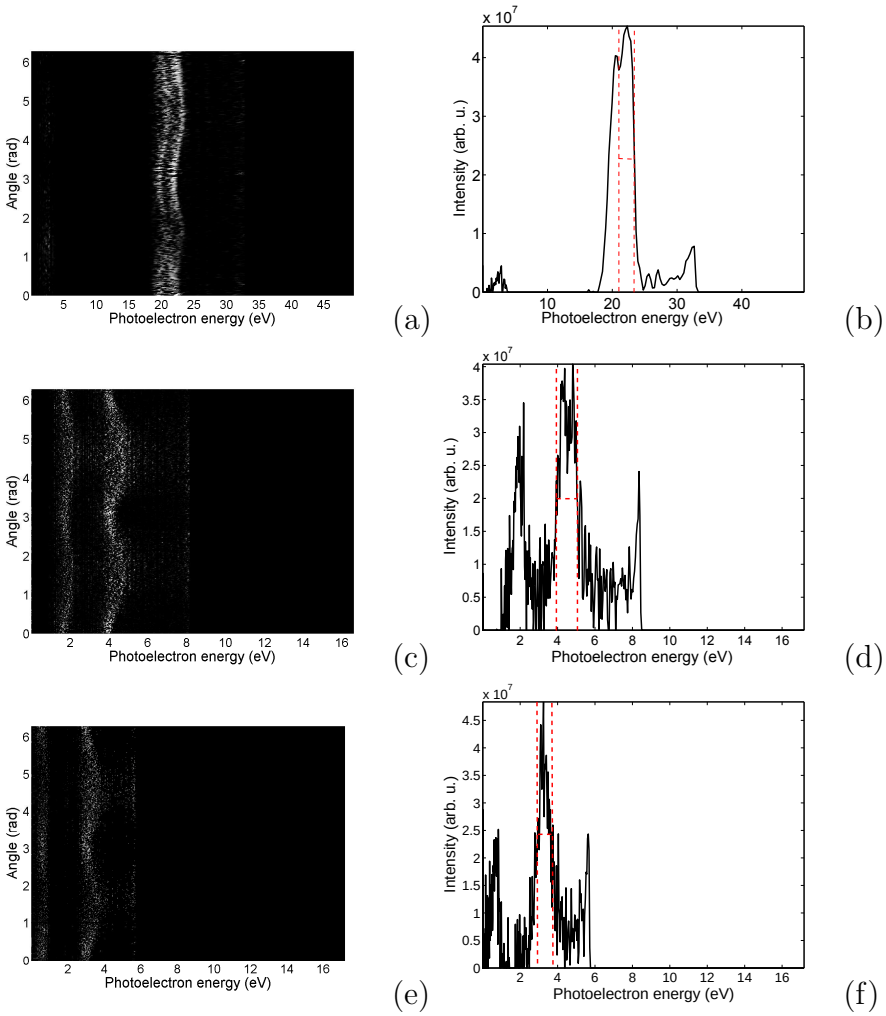

Figure 3.2: The polar representation of the inversion obtained at a photon energy of a) 270.6 eV c) 252.6 eV e) 251.6 eV and the respective plot of image intensity against photoelectron kinetic energy given by b), d) and f). The vertical red, dashed lines indicate the maximum and minimum values of the photoelectron kinetic energy, determined from the FWHM (horizontal dashed line).

For the 252.6 eV and 251.6 eV plots, the two distributions are well resolved by kinetic energy. The spectra are very noisy but it is possible to separate the two distributions. At the 270.6 eV energy however, the two peaks overlap and cannot be identified individually. This makes it challenging to determine the kinetic energy region in which to measure the angular distribution and it may have an affect on the value determined for the asymmetry parameters at this energy. The energy resolution of the $2p_{3/2}$ distribution at each photon energy has been measured and presented in table 3.1.

Photon energy (eV)	Δ E_k(FWHM) (eV)	Peak E_k(eV)	R=ΔE_k /E_k
270.6	23.4-21.1 = 2.3	22.3	0.1
252.6	5.1-3.9 = 1.2	4.4	0.3
251.6	3.8-2.9 = 0.9	3.3	0.3

Table 3.1: The energy resolutions (R) of the $2p_{3/2}$ distributions. Δ E_k (FWHM) is the difference between the maximum and minimum kinetic energy determined from the FWHM and E_k represents the central kinetic energy of the $2p_{3/2}$ peak from the intensity plots.

The resolution in the energies close to threshold are marginally better than for the highest photon energy, which seems to indicate that even though the distributions are well resolved, the noise in the inversion is having an affect on the inversion image quality. At the lower photon energies though, the distortions in the lines are not as prominent as they are in the 270.6 eV image but they do suffer from more blurring on the $2p_{3/2}$ line, particularly at $\theta = \pi/2$ and $\theta = 3\pi/2$. The values indicate that the energy resolution should be improved, as a typical value of a few percent for R is achievable by the VMI [7].

The values of the asymmetry parameter obtained from the fitting of equation 1.10 to the energy distribution of the $2p_{3/2}$ state photoelectrons in each polar image are presented under the 'measured' heading in table 3.2

Photon energy (eV)	β for $2p_{3/2}$	
	Measured	Avaldi
270.6	0.39 $\pm$ 0.07	$\sim 0.37 \leq \beta \leq 0.46$
252.6	-0.19 $\pm$ 0.03	$\sim 0.17 \leq \beta \leq 0.29$
251.6	-0.14 $\pm$ 0.04	$\sim 0.33 \leq \beta \leq 0.43$

Table 3.2: A comparison of the measured and pre-existing values for the asymmetry parameter from Avaldi [32] at the investigated photon energies.

The values of β vary quite significantly for the 270 eV energy image and the threshold images. They are all intermediate values (values between +2 and -1) but those determined for the near threshold energies are negative. The error associated with each measurement is statistical and has been determined by the curve fitting feature in the Matlab package. The intermediate values measured imply that the εs and εd partial waves of the emitted photoelectrons have interfered, resulting in the photoelectrons being emitted at angles that are neither in line or at right angles to the transition dipole moment.

A study by Avaldi *et al.*(1994) [32] extended the Lindle ionisation studies of the Ar 2p shell by measuring the β parameter at energies even closer to threshold. The work measured the asymmetry parameter for photoelectrons between 0.25-30 eV, and also measured it for both the $2p_{1/2}$ state and the $2p_{3/2}$ state, which previously had not been done. Table 3.2 shows the values of β measured in that study for the same photon energies used in this investigation.

A comparison of the findings show that for the 270.6 eV photon energy, the value of β concurs with the pre-existing, experimentally determined value within statistical limits. The Avaldi values have a minimum and maximum range due to the errors associated with the experimental measurements based on a conventional spectrometer. Most obviously in the results of Avaldi, there is a variation in the value of β as a function of energy.

This was explained by Avaldi as being due to intrachannel coupling between the εs and εd ionisation channels of the 2p shell. At energies just above threshold, the 2p $\rightarrow \varepsilon$s channel is perturbed by the stronger 2p $\rightarrow \varepsilon$d channel. Its phase shift and or its matrix element would be altered as a result and ultimately, so would the asymmetry parameter. The physical interpretation of the perturbation of these channels was described by Schmidt (1992) [22] as a Post Collision Interaction (PCI) effect. A description of how such effects arise in Argon is now described. The ionisation of a Ar 2p photoelectron, ultimately leads to the rearrangement of the ion core with a possibility of there either being a radiative or non-radiative decay of the newly created inner shell hole [22]. For Argon the most likely non-radiative decay process is given by

$$h\nu + Ar \rightarrow Ar^{+} + e^{-} \rightarrow Ar^{++} + e^{-} + e_{A}^{-}$$

where Ar^{++} is a doubly charged ion (primarily in its $3s^2 3p^4(^3P,^1D,^1S)$ states and partially in the $3s3p^5(^3P,^1P)$ [40]) created by the release of an Auger electron e_A^-.

In this process, the release of the photoelectron (e^-) leaves a singly ionised core (Ar^+), but at photon energies just above the L-shell threshold, the

low amount of energy the photoelectron possesses normally results in the time for this photoelectron to leave the atom being larger than the time for the rearrangement of the remaining electrons surrounding the newly created vacancy. Thus, this subsequent decay of the inner shell hole produces an Auger electron with a velocity that exceeds that of the photoelectron. The photoelectron experiences less screening of the nucleus, due to being exposed to doubly ionised core, and is loses energy. Consequently the Auger electron experiences the effectively smaller potential of a singly ionised core and gains energy. This exchange in the mutual screening and energy of the outgoing photoelectron and Auger electron is interpreted as a post collision interaction [40][41][22].

The β result obtained at a photon energy of 270.6 eV suggests that such interactions have successfully been 'observed' upon the ionisation of the 2p Ar shell with soft X-ray radiation by the imaging XPS technique, and that the complete photodynamical information of the photoprocess at this energy has been extracted from the reconstructed 3D velocity distribution obtained in this novel approach.

In regards to the photon energies close to threshold, the values of beta determined are substantially different from those of Avaldi. At such low photon energies it seems that the amount of background in the raw VM-image has a huge influence on how successfully the asymmetry parameter is determined. Even though background subtraction was implemented it was not sufficient enough to reduce the effect the remaining background had on the fitting of the angular distribution. However, a VMI spectrometer allows access to much lower photoelectron kinetic energies than can be reached by conventional spectrometers. It is very clear from the VM-images and the photoelectron distributions within them, that low photoelectron kinetic energies can be measured and successfully inverted; it is merely the amount of background within the raw images, at least in this case, that is the main limitation in the analysis of them and therefore, if more effort is made to reduce such effects, then the imaging XPS technique may be very powerful in this experimental situation.

3.2 Photoionisation Dynamics in Molecular N_2O

It was realised in the study of Argon, that the energy resolution of the inversions could be a possible limiting factor in the accurate determination of the β parameter. The difficulty experienced in completely resolving the two distributions is possibly due to the 2.2 eV kinetic energy difference that separates the two states being too small for good resolution. To resolve this problem, the N_2O molecule has been chosen to be investigated.

The N_2O molecule has a linear geometry of N_t-N_c-O in the neutral ground state, where N_t and N_c represent the two, non-equivalent terminal and central Nitrogen atoms respectively [42]. Ionisation of the N 1s state results in the emission of photoelectrons from the core 1s levels of both the N_t and N_c atoms; The ionisation thresholds of these atoms, as documented by Ehara *et al.*(2011) [42], are 408.43 eV and 412.44 eV respectively, therefore the photoelectrons ejected from these orbitals upon ionisation are separated by a 4.1 eV difference. This energy separation is caused by shifts in the binding energies of the atomic orbitals that are induced by the two different Nitrogen atom environments, N_t - N_c and N_c - O. As there is a greater difference in energy between the distributions, the energy resolution of the images should be improved and therefore so should the accuracy in determining the asymmetry parameter.

Before conducting ionisation studies, NEXAFS was carried out on the N_2O molecule at energies close to the Nitrogen K-shell ionisation edge. The spectra obtained is shown in figure 3.3.

The two most prominent peaks in the spectra correspond to the N_t $1s \longrightarrow 3\pi*$ and the N_c $1s \longrightarrow 3\pi*$ transitions [43] and occur at photon energies of 401.1 eV and 404.7 eV respectively [44]. The $\pi*$ orbital is the lowest unoccupied molecular orbital which a core electron can make a transition to. The ionisation thresholds of the terminal and central Nitrogen atoms and their positions in relation to the NEXAFS spectra, are shown by the blue and green lines present in figure 3.3. As there is not much data after the threshold of N_t it is not possible to see the Rydberg states in the continuum of the N_c atom. However, Rydberg states present below this threshold are clearly visible and even though the resolution is limited by the slit width, it is still possible to discern which states the peaks correspond to. In accordance with the peak identification of Ehara *et al.*(2001) the peak arising at 406.3 eV represents the transition of a core electron, from the terminal Nitrogen atom, to the $3p\pi$ Rydberg state. The peak at 407.4 eV, close to the N_t threshold, corresponds to a transition to either the $5s\sigma(N_t)$ or the $4p\pi(N_t)$ state.

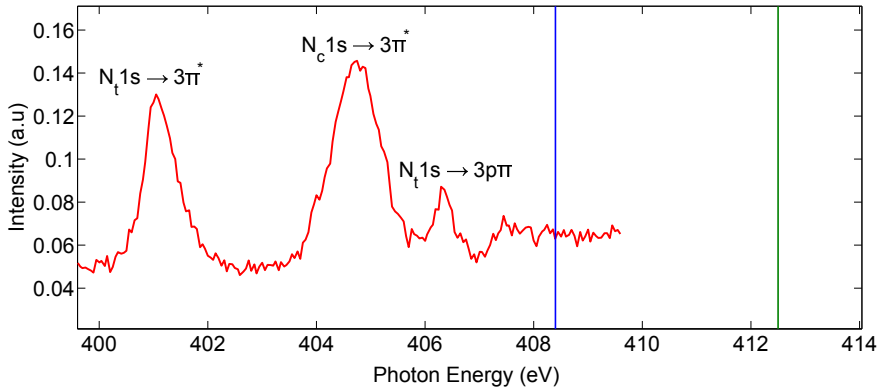

Figure 3.3: The NEXAFS spectra near the Nitrogen K-shell of N_2O. The red line indicates the N_2O absorption data. The blue line marks the threshold energy of the N_t atom at 408.4 eV while the green line marks the threshold energy of the N_c atom at 412.5 eV.

The ionisation studies on the N 1s state were performed at photon energies of 420.6 eV, 430.6 eV and 437.6 eV and the resulting corrected VM-images and their corresponding inversions are shown in figure 3.4.

In all of the images the photoelectron distributions from the two N atoms are visible. As the ionisation threshold is lower for the N_t atom, the outer photoelectron distribution observed in a VM-image correspond to ejections of particles from the 1s orbital of this atom. The photoelectron distributions at all energies, appear to have preferential ejection along the direction of the polarisation, as the greatest intensity is seen at $\theta = 0$ and $\theta = \pi$. There is still however a small amount of photoemission in the horizontal direction to $\hat{\mathbf{E}}$ which is seen most clearly within the 430.6 eV image.

Like in the case of Argon, the VM-images from all of the investigated energies are affected by background signal. This is most prominent in the 420.6 eV image (figure 3.4e) which is closest in energy to the thresholds of the Nitrogen atoms in the molecule. Most of the signal interferes with the N_c photoelectrons at an angle of $\theta = \pi/2$. This is carried through into the inversion and it is seen in this image that the noise it is not focused towards the centre, but is situated close to the inner N_c ring. Because of this interference, the β value for the N_c atom has not been reported. However in comparison to Argon, in the VM-images of N_2O there is an obvious visual distinction between the two photoelectron distributions. There is still slight blurring of both the rings, most noticeable at $\theta = \pi$, that is carried through into the inversion, but the distributions are very well separated at all angles.

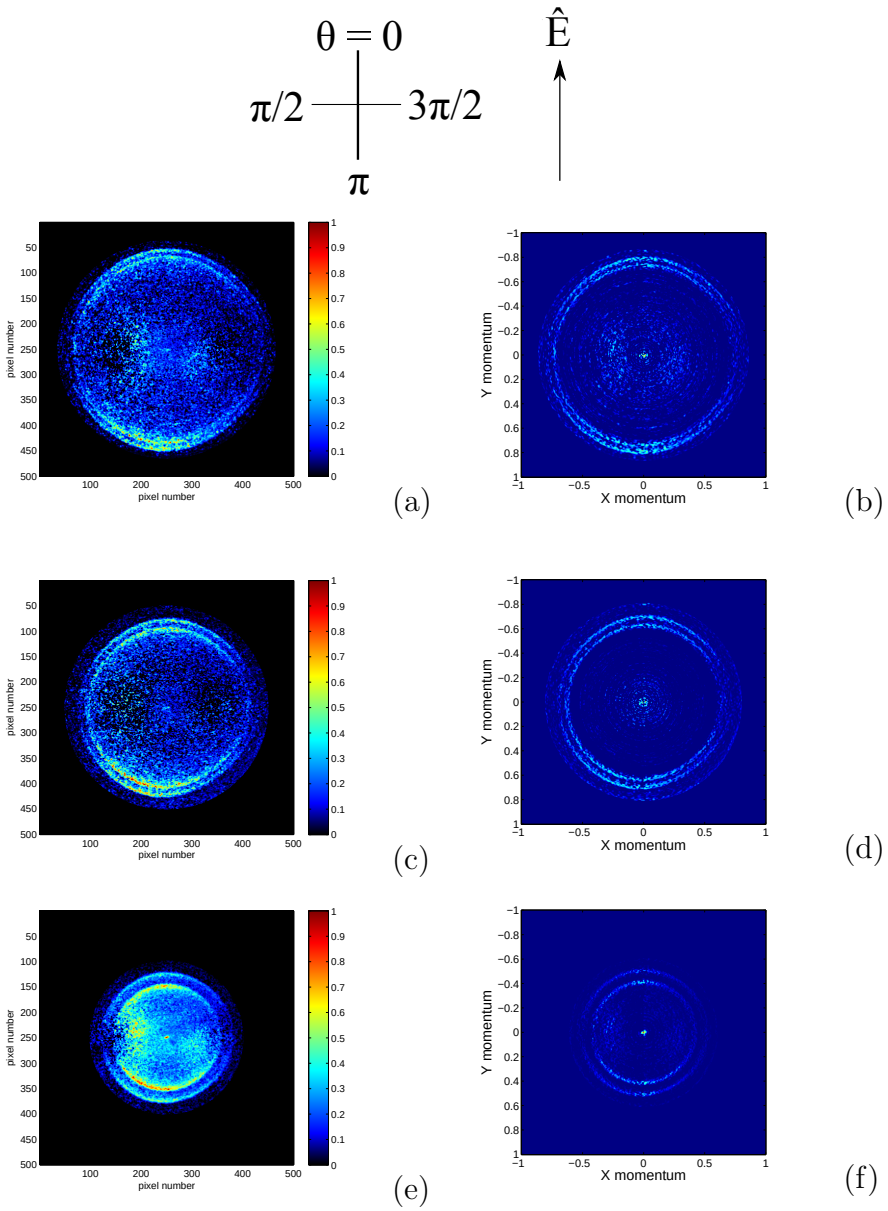

Figure 3.4: The optimised VM-images obtained from the ionisation of the N_2O N 1s shell at a) 437.6 eV b) 430.6 eV and c) 420.6 eV, with images b), d) and f) being their respective inversions. The angle within the images is shown by the axis, the direction of the polarisation vector with respect to all the images is given by the vertical arrow above the images.

This leads to sharp rings in the inversion, which should increase the accuracy in the selection of the complete angular distribution information of the N_t photoelectrons, on which to model the differential cross section.

In order gauge the true extent of the improvement in the energy resolution, the inversions represented in polar form and their corresponding intensity plots as a function of kinetic energy are shown in figure 3.5.

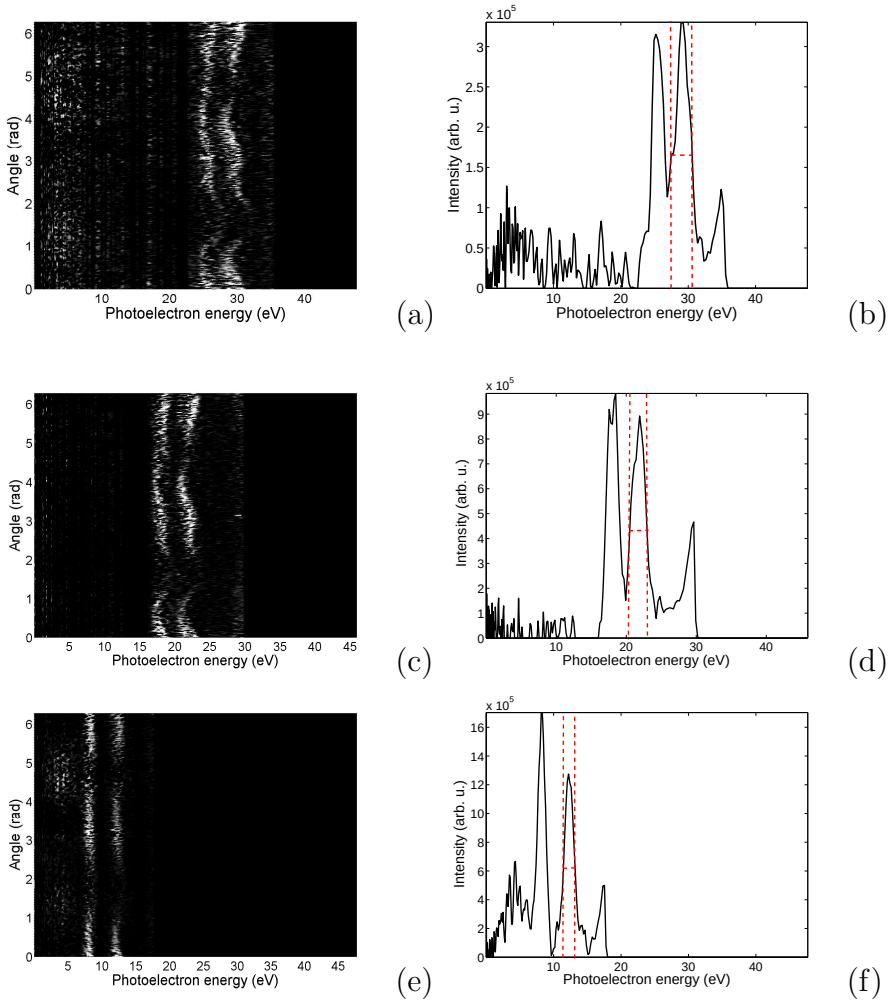

Figure 3.5: The polar representation of the inversion obtained at a photon energy of a) 437.6 eV c) 430.6 eV e) 420.6 eV and the respective plot of image intensity against photoelectron kinetic energy given by b), d) and f). The vertical red, dashed lines indicate the maximum and minimum values of the photoelectron kinetic energy determined from the FWHM (horizontal dashed line).

In each polar image, it is clear to see two distinct horizontal stripes representing the photoelectrons from the N_t and N_c 1s states. The horizontal stripes suffer a lot less blurring than the Ar images, especially the outer line from which β is be extracted. Figures 3.5a and c still suffer from image distortions but figure 3.5e shows two almost perfectly straight lines, which means that the mapping of identical photoelectrons with respect to their kinetic energy has successfully been achieved and is reflected through the inversion. The intensity plot also reflects the quality of this inversion as the two peaks representing the N_t 1s and N_c 1s photoelectron distributions are completely resolved. The peaks in figures 3.5b and d do overlap, but they are resolved to an extent such that it is possible to identify which distribution they represent. What is noticed from the intensity plots of N_2O is that the noise which affects the resolution of the peaks in figures 3.2 d and f, is not present at these photon energies. Table 3.3 shows the energy resolution of the N_t peak determined at at each photon energy.

Photon energy (eV)	Δ E_k(FWHM) (eV)	Peak E_k(eV)	R=ΔE_k /E_k
437.6	30.6-27.5 = 3.1	28.9	0.1
430.6	23.0-20.6 = 2.4	21.9	0.1
420.6	13.3-11.5 = 1.8	12.2	0.15

Table 3.3: The energy resolutions (R) of the N_t distributions. Δ E_k (FWHM) is the difference between the maximum and minimum kinetic energy determined from the FWHM and E_k represents the central kinetic energy of the N_t peak from the intensity plots.

The β values obtained from the angular distributions of the N_t 1s state for the different energies are presented in table 3.4 under the 'measured' column.

Photon energy (eV)	β for N_t		
	Measured	Lucchese (DA)	Guillemin (non-DA)
437.6	1.62 $\pm$ 0.16	$\sim$ 1.7	$\sim$ 1.88
430.6	1.21 $\pm$ 0.12	$\sim$ 1.6	$\sim$ 1.77
420.6	0.84 $\pm$ 0.09	$\sim$ 1.0	$\sim$ 1.20

Table 3.4: A comparison of the measured and pre-existing values for the asymmetry parameter as deduced by Lucchese [45], in the regime of the dipole approximation and by Guillemin [46], in the regime of non-dipole approximation at the investigated photon energies

From the results it can be seen that the measured asymmetry parameters decrease in value with decreasing photon energy. They all take on values between +2 and -1 implying that at each energy, that transitions are neither purely parallel or purely perpendicular. However, the value of beta measured relative to these two extremes, represent the extent to which the two types of transition are mixed. In the case of the 437.6 eV energy the value of $\beta = 1.62$. As this value is close to two, it suggests that most of the photoelectrons are ejected in the direction of the polarisation vector but with a fraction also emitted perpendicularity to it. For $\beta = 0.84$ the preferential direction for ejection is still in the vertical axis but now there is a greater amount of ejection in the perpendicular direction that contributes to the overall angular distribution. To some extent this can be witnessed in the inversion images, as for decreasing photon energy, there is as increase the intensity of the photoelectrons at the angle $3\pi/2$ and so therefore also at $\theta = \pi$, as the inversion is symmetric.

The β values - as a function of photon energy - for the N_t 1s photoelectrons in the dipole approximation have previously been documented by Lucchese *et al.*(2007) [45] and the results of their studies can also be found in table 3.4. The values of Lucchese are estimated because the results do not separate distributions from the two 2p subshells; the errors associated with these measurements are not provided in the paper.

The β values measured in this investigation are lower than that given by Lucchese, with only the 437.6 eV result coinciding to the documented value within statistical error. However as the Lucchese values are approximate, it is possible that they could deviate from the reported value to an extent such that they coincide with the results of this investigation. Thus it seems reasonable to assume they concur.

This is a vast improvement in the successful determination of the β values in comparison to that of Argon, which does suggest that not only is the value measured influenced by the amount of background signal present in an image but also on the capability of the spectrometer and the analysis procedure to successfully resolve energies lower than 4 eV.

The determination of these β values was based on the assumption that the dipole approximation was valid in the soft X-ray regime provided by a synchrotron light facility. It is known that for high photon energies (>5 keV) the purely dipole approximation does not hold and that full expansion of equation 1.8 is required to successfully explain the differential cross section [47]. For low photon energies in the UV range the DA is considered as being completely upheld, as relativistic effects are rendered unimportant in this region and the wavelength of the UV radiation is larger than the Bohr radius from which electrons are ejected [48]. But it has also been observed that

within soft X-ray region, non-dipole corrections to this approximation have to be considered and even though the effects are not as great at such low energies, they still contribute to the resulting angular distribution of the photoelectrons.

Such observations were documented by Jung *et al.*(1996) [19] who investigated non-dipole effects using tunable, polarised light in the 2-5 keV energy range. It was found that in this range, the dipole approximation assumption no longer holds and prominent energy-dependent asymmetries in the angular distributions of the photoelectrons with respect to the direction of photon propagation are observed; these effects were dependent on atomic number and the orbital angular momentum of the photoemitted electron. The observations were found upon ionisation the of s subshell in simple physical systems and it was noted that further work was needed both experimentally and theoretically to extend the scope of this research to more complicated systems. These findings questioned the validity of the DA assumption in the soft X-ray region and raised the issue of what effect it would have on XPS measurements and therefore on the applications, such as gas phase studies, that are dependent on it [46].

Work conducted by Guillemin *et al.*(2006) [46] attempted to gain insight into such queries by investigating non-dipole effects in molecules in gas phase. In particular they studied the effects upon the ionisation of the N 1s shell of the N_2O molecule, using soft X-rays from a synchrotron source, and determined the dipole (β) and non-dipole asymmetry parameters for both the N_c and N_t atoms. The results of β found for the N_t 1s state are presented in table 3.4. According to the results of Guillemin, the values of β determined in the Lucchese paper have been underestimated, as they have not taken into consideration the non-dipole asymmetry. The results of this study give values of the asymmetry parameter that are similar to that of Lucchese implying that the dipole approximation is valid, but as such effects have been witnessed in the N_2O molecule under the same experimental conditions of this work, which include synchrotron radiation in the soft X-ray range and gas phase targets, it seems evident that non-dipole effects would be present and possibly observable and therefore should be investigated.

The inclusion of non-dipole effects results in the complete expansion of equation 1.9 to include the higher order electric quadrupole (E2) and magnetic dipole (M1) interactions. In the case of soft X-rays an expansion to the fist order correction, which takes into account the non dipole effects in a perturbative manner [18] are usually adequate; this has been supported by the agreement between calculations obtained in the first order non-dipole framework and experimental data on atoms [48].

In this first order correction, these higher order terms contribute through

cross terms with the electric dipole (E1) amplitude and they do so in such a way that leave β and θ_{total} unaffected, but that lead to forward and backward asymmetries in the angular distribution of photoelectrons with respect to the direction of propagation of the light, **k**. In the soft X-ray range, the E1-E2 cross terms cause the biggest deviations from the DA and at this level of approximation, two new non-dipole angular distribution parameters and an azimuthal angle, ϕ (see the coordinate axis in figure 2.6) can be incorporated into the photoionisation differential cross section (equation 1.10). The resulting form, as given by Cooper (1993) [18], of the differential cross section in the first order non-dipole approximation for 100% linearly polarised light, is written as

$$\frac{d\sigma}{d\Omega} = \frac{\sigma_{total}}{4\pi}[1 + \beta P_2(cos\theta)] + (\delta + \gamma \cos^2\theta)\sin\theta\cos\phi \tag{3.1}$$

The non-dipole parameters δ and γ can be expressed in terms of radial matrix elements and their relative phases and are dependent on subshell and photon energy. They are related by the relationship $\zeta = \gamma + 3\delta$, where ζ represents the non-dipole angular distribution.

The inclusion of these parameters, which account for asymmetry in the measured angular distributions of photoelectrons, essentially means that the symmetry in the polarisation axis, which the iterative inversion procedure needs in order to perform properly, is broken; therefore it can not be used to determine if non-dipole effects are present. Instead equation 3.1 was modelled to the 2D distributions in the corrected VM-images. This was done by converting the corrected Cartesian images into polar images without carrying out the iterative inversion.

In order for the curve fitting tool to accurately model this equation to the data, the value of β had to be fixed. As it has been assumed that the β values have been underestimated in this study if non-dipole effects are present, the values were fixed to were that of Guillemin presented in table 3.4. As delta and gamma are only corrections of the DA the value of beta should remain constant. The ζ values calculated, upon the extraction of the non-dipole asymmetry parameters, are presented in table 3.5. The corresponding non-dipole angular distributions recorded by Guillemin at these energies are also presented in table 3.5.

Photon energy (eV)	Measured			Guillemin
	δ	γ	ζ	ζ
437.6	0.42 ± 0.08	-1.55 ± 0.31	-0.29 ± 0.39	~ 0.73
430.6	0.53 ± 0.11	-0.92 ± 0.46	0.67 ± 0.57	~ 0.73
420.6	0.37 ± 0.08	0.23 ± 0.36	1.34 ± 0.43	~ 0.53

Table 3.5: The measured non-dipole asymmetry parameters and the corresponding parameters as measured by Guillemin [46].

The values of ζ obtained in this study vary extensively for the different photon energies and they have large errors associated with them, whereas the Guillemin values at these photon energies are rather similar. The result of ζ obtained at a photon energy of 430.6 eV, does have a value that is within the error limits of this equivalent pre-documented one. The variation in the asymmetry parameters and their divergence from the Guillemin quantities, may be due to the fact that the differential cross section in the non-dipole regime was modelled to the 2D projections rather than the 3D reconstruction and even though there is a relationship between the two, it may not be sufficient enough to accurately observe the small non-dipole effects that possibly occur. The errors associated with the data points in the Guillemin studies are unknown, but at all photon energies there is at least a 0.1 eV range that a determined β value can vary between.

Non-dipole effects have been witnessed in the N_2O molecule under the same experimental conditions, but from the values of ζ in this instance it is not possible to conclude that these photoionisation dynamics have been exposed by the imaging XPS technique. Being able to have witnessed the non-dipole effects in this novel way would have given greater insight into processes that happen intrinsically within the N_2O molecule; this is of great significance because as of yet there is very little known about molecular non-dipole effects and there is no theory to describe the effects in N_2O.

3.3 Photoionisation Dynamics in FePc

The ultimate goal of this investigation was to successfully combine VMIS and XPS in order to investigate the photoprocesses that occur in complex molecules, in particular for those that occur upon ionisation of core electrons in phthalocyanines (Pc's).

These have become molecules of great interest because of their interesting applications [8][9][10][11]. There have been studies both theoretical [49] and experimental on the ionisation of valence electrons from these complex molecules, but most experimental studies are concerned with the Pc's when adsorbed on substrates [50][51]. Shake up excitations [52] and satellites that have been seen to occur in the spectra of these molecules, could then be a result of them being adsorbed on substrates rather than being intrinsic of the molecule themselves. Therefore studying the ionisation of core electrons from these complex molecules in gas phase would be an interesting area of study in which to apply the technique and to get conclusive evidence as to whether the phenomena witnessed previously, are associated purely with these molecules or not.

In this investigation gas phase iron phthalocyanine (FePc) was chosen to be studied. Investigating the photoionisation dynamics of the simpler N_2O molecule was intended as a provision to understanding the VM-images and the underlying photoprocesses that occur in the more complex FePc molecule, thus aiding in the interpretation of the photodynamics within this molecule and whether or not these intrinsic processes give rise to the features seen in the spectra of other works.

Solid Sample Sublimation Source

The VMI spectrometer is limited to the analysis of gas-phase substances. Thus in order to investigate the reaction dynamics of the solid FePc sample, a sublimation source in the form of an oven was developed. The oven heats up until the vapour pressure inside it is such that it allows the expansion of a gas in a vacuum.

The oven shown in figure 3.6 was heated by a Rollmax 3,3 x 3,3 provided by Backer. The main heating element is a nickel/chromium resistive wire but integrated into the system is a J-type thermocouple that monitors and controls the temperature. The oven was mounted vertically, underneath the main chamber of the VMI spectrometer. The oven was fixed to an extension rod of length 28 cm which was connected to a translator; this allowed the translational motion of the oven, in and out of the main chamber, to be

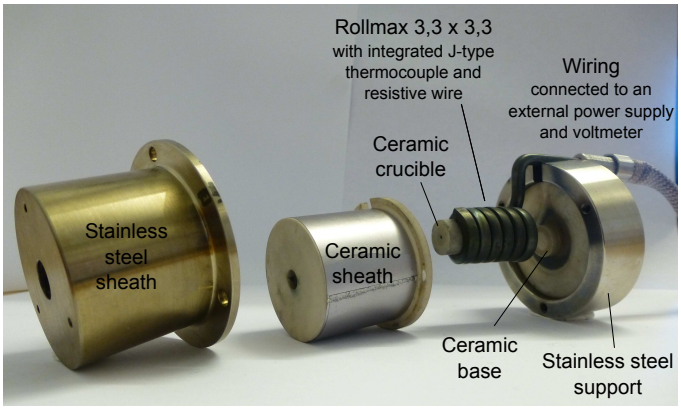

Figure 3.6: Picture of the oven showing the individual components of which it is comprised. The coil of the Rollmax fits around a ceramic crucible which contains the FePc sample under investigation. The sublimed solid leaves the crucible through a 1mm aperture. Both the coil and the crucible are held in place by a ceramic base that sits in a hollow stainless steel support. The metal base has a segment cut out of it in order to compensate for the straight length of the Rollmax. A ceramic sheath, with a 5mm exit slit in its top end, envelopes the coil and the crucible. A protective stainless steel sheath, also with a 5mm diameter opening in it top end, covers the ceramic layer. It fastens to the metal base ensuring that all of the inner components of the oven are completely encased and therefore making it an isolated system.

manipulated manually. The oven was connected to an external voltage supply that provided power and to a voltmeter, so that the temperature inside the oven could be determined from the corresponding voltage given by a generic J-type thermocouple calibration curve.

The oven chamber was isolated from the main chamber by a valve, so that the oven could be installed without affecting the vacuum pressure. When the vacuum inside the oven chamber was comparable to that in the main, the valve was opened and the oven lifted until there was only a 1 cm gap between the top of the oven metal sheath and the photon beam.

For the measurements, the crucible was completely filled with FePc sample and to ensure that the sublimation point of the FePc was achieved, the oven was heated to around to 460^oC. However the point of sublimation and degradation for FePc are separated by a temperature of approximately 50^oC and this became problematic upon heating the sample. The way the heat was transferred through the crucible to the sample was effected by the amount contained within the crucible. Because of the pure volume, the inner and outer regions of the sample heated at different rates and ultimately resulted

in both the sublimation and degradation points being reached. Such problems have been reported in the heating of guanine for similar experimental work and it had been suggested that better results are achieved with small amounts of sample [53].

As well as this, there was approximately a 100^oC temperature gradient between the outer metal casing and the inner ceramic component of the oven. Thus when the gas phase FePc molecules passed through the opening at the top of the ceramic crucible, upon contact with the casing, they immediately cooled resulting in a build up of solid FePc around the openings, preventing any gas from entering the spectrometer. This problem occurred at the very end of the available beam time and as a result of time constraints no FePc data was obtained.

Conclusion and Outlook

The useful dynamical information that can be extracted from the angular distributions of photoelectrons obtained upon inversion of raw VM-images, is affected by the quality of the inversion image and on the geometry under which the raw VM-image is obtained. The determination of the asymmetry parameter is affected by how much background signal is present in the raw VM-image and its position in relation to the key features within it, which in turn is dependent on the photon energy.

Most of the background, contained within both the Ar and N_2O images, has been positioned close to the image centre, but as the photon energy decreases so does the kinetic energy of the photoelectrons and therefore so does the radius of their distributions. At energies close to threshold where the photoelectrons have a few eV of energy, the radius of the rings are small and are subsequently situated in the location of the background. This effects the extraction of the β parameter at these energies as the background influences the photoelectron signal from which it is measured. All of the images were subject to background subtraction before being inverted, but it was not always sufficient enough to remove all the noise especially at near threshold energies. However even with the noise present it is obvious that the VMI spectrometer, used for the imaging XPS technique, can 'capture' the velocity distributions of photoelectrons with low kinetic energies produced upon the ionisation of inner shells induced by soft X-rays, meaning that the determination of β from the angular distributions of slow moving photoelectrons is highly likely if more effort is made to reduce the amount of background signal created in the spectrometer, as it is not possible to reduce it enough in the analysis procedure.

The inversion images for both Ar and N_2O were subject to distortions that were carried through from the collected, raw VM-images. This did have an effect on how accurately β was deduced from the reconstructed angular distributions on which the differential cross section was modelled, as the image distortions influenced them. Thus, in this investigation the accuracy and reliability of the β values may not be as good as what is possibly

achievable with the spectrometer i.e, with the use of laser light, but the distortions are as a result of skewing in the detector plane caused by residual aberrations of the spectrometer electrostatic lens, which is an issue caused by the experimental set-up. Therefore in the future setting up the equipment with the highest precision could eliminate this problem.

Due to such issues, it was not possible to observe the same trends in the asymmetry parameter of Ar at the investigated photon energies as have been documented previously. However the imaging XPS technique was successful at determining β for the highest photon energy used to probe the photodynamics of Ar. This implies that even in the case of soft X-rays, the quantum mechanical interference effects between the outgoing ionisation channels are successfully 'captured' by imaging XPS, which makes it an extremely powerful tool.

In the N_2O images however, the extracted β values concurred with previously documented results. The photon energies studied were further away from the N_t 1s threshold energy than the energies used to study Ar but they were still at most only 29.2 eV above the energy threshold of the N_t 1s state. It appears that the improvement in the measurement of β in N_2O, is due to the 4.2 eV energy separation in the kinetic energies of the photoelectrons from the ionised 2p states and this indicates that the capability of the technique may be limited by its resolving power in a synchrotron facility.

From these outcomes it seems plausible that the imaging XPS technique can be used in conjunction with synchrotron light in order to successfully measure the photoionisation dynamics in atoms and molecules, but the issues arising due to image distortion and background signal need to be eliminated first in order to obtain accurate values of the dipole asymmetry parameter. Both the spectrometer and the imaging technique allows access to kinetic energies of photoelectrons that are not accessible with many other spectrometers and so it is important for future work that these problems that affect the images are resolved.

The major limiting factor of the procedure is that the iterative inversion requires symmetry in the raw VM-images in order for them to be inverted with a good quality. As has been reported within this investigation, the experimental conditions on which a measurement of β has been obtained could induce effects that cause asymmetry in the images. The inversion procedure is not equipped to account for these effects and its inability to do so could result in vital information on the photodynamics being lost. This is extremely detrimental for works that use this analysis procedure to look at the photodynamics of not so well studied systems.

One solution to this could be to use a Monte Carlo simulation to create a replica of the final inversion. The dipole and non-dipole asymmetry pa-

rameters could be input into the program and changed accordingly until the Monte Carlo simulated inversion produces a result that is exact within error limits to the experimentally obtained inversion.

However this would only solve the asymmetry problem in the images and not any of other effects. One idea that could possibly solve all of the issues, is to use the slice imaging as reported by Rakitzis *et al.* [7]. This method allows for the direct measurement of $\frac{d\sigma}{d\Omega}$ from a slice image of the 3D velocity distributions without the need of an inversion technique. The method is general and can be used not only for photoelectron imaging, but for reaction product imaging also. The elimination of the image analysis would not only get rid of the blurring and the distortion seen within inversion images, but it would also mean that non-dipole effects may also be seen, ensuring that a complete dynamical picture of the photoionisation process is seen.

The ultimate goal of studying FePc was not achievable during this investigation. However the problems that arose during these studies are rectifiable and so it would be more than possible for future works to pursue such research. A simple solution could be to load less sample in the crucible so that a more even heat distribution is achieved across the sample; this would eliminate the issue of inhomogeneous heating and therefore the problem of both sublimation and evaporation of FePc occurring simultaneously. Also, heating up the oven more slowly may result in the temperature gradient across the inner and outer components of the oven being diminished. Another possible solution could be to improve upon the oven design, such as removing the metal casing material or by changing the size of the openings for example.

Self Reflection

Looking back over the time of my thesis study, I realise how much I have learnt and how much I have progressed, not only a scientific level but on a personal level also. The journey to complete my thesis work has not necessarily been the smoothest; in my opinion I have faced a lot of adversity and I am very proud to say that I managed to push through all of it and create a piece of work that was my own and survived to tell the tale.

During the course of my study I had to overcome many challenges, the biggest being my computer illiteracy. The thesis required the use of a Matlab code that had little operating instructions provided with it and that was completely new to me. This, alongside my inability to read and understand computer coding made the thought of conducting any work with it very daunting. However from this work, I have gained an understanding of computer coding, I have learnt how to diagnose problems within a code and manipulate them according to my needs. In fact, I dare say that I came to enjoy this aspect of my work as I found great satisfaction in finding a problem, being able to solve it and then reaping the rewards of your efforts when something functioned as it should. I feel that I have become proficient in the use of this particular program and I feel that if I continued to practice with Matlab and coding in general, my confidence and abilities in programming would continue to grow.

I was very unfortunate that whilst writing my thesis three computers stopped functioning for various reasons. The most devastating of these malfunctions resulted in the loss of my hard-drive, which contained all of my results. However, through losing this information and therefore having to reproduce it, I found an error in the code I was using to analysis my results that I would not have noticed otherwise and through finding it I was able to improve my results drastically. This in itself was a great lesson, proving that at even the most challenging times, with determination and the right attitude, any negative can become a positive.

I have learnt a lot of new things during my thesis work that I know I will use in future ventures. During my beamtime at MAX-lab I gained numerous

practical skills and insight into the amount of effort that goes into having a successful beamtime. I thoroughly enjoyed being part of a team effort and I felt privileged to have the opportunity to work at such a renowned national facility. I enjoyed being given personal tasks, mainly in regards to the development of the oven, as it gave me a sense of independence and value. In order to write my thesis, I have had to learn how to use various computer programs that I would never have learnt to use otherwise. These include Lyx, Latex, Adobe illustrator and Inkscape and what I have learnt about each of them will be beneficial to me in many aspects of work.

Most importantly, I have gained knowledge and insight into an interesting area of work. Applying imaging XPS as it was during this investigation, with the use of a VMI spectrometer on a soft X-ray beam was a novel approach and I understand that my department were the first to initiate such an investigation. It is extremely exciting to think that the studies I conducted could be used to help develop works of this kind in the future. From reading numerous journals and books and from the writing process itself, I feel that I have a good grasp on my thesis work and I know that my knowledge in this field of work has improved leaps and bounds from when I started, which is extremely satisfying.

The greatest thing I have learned through out this whole process is that I can do anything I put my mind to. I am more than capable of achieving my goals, all it takes is a little engagement and a focused mind set. I have realised that I am competent physicist and that I should have confidence in my scientific abilities and in myself. There will always be challenges, always something new to learn, always a time when you question yourself and always room for improvement, but as long as you do not give up, you can not fail.

Bibliography

[1] K. M. Siegbahn, "Nobel Lecture: Electron Spectroscopy for Atoms, Molecules and Condensed Matter," *Nobelprize.org*, Nobel Media AB 2013. Web.3 June 2014.

[2] U. Gelius, E. Basilier, S. Svensson, T. Bergmark, and K. Siegbahn, "A High Resolution ESCA Instrument with X-ray Monochromator for Gases and Solids ," *Journal of Electron Spectroscopy and Related Phenomena*, vol. 2, no. 5, pp. 405 – 434, 1973.

[3] C. S. Fadley, "X-ray Photoelectron Spectroscopy: Progress and Perspectives ," *Journal of Electron Spectroscopy and Related Phenomena*, vol. 178–179, no. 0, pp. 2 – 32, 2010. Trends in X-ray Photoelectron Spectroscopy of Solids (Theory, Techniques and Applications).

[4] J. Cooper and R. N. Zare, "Angular Distribution of Photoelectrons," *Journal of Chemical Physics*, vol. 48, 1968.

[5] J. Söderström, N. Mårtensson, O. Travnikova, M. Patanen, C. Miron, L. J. Sæthre, K. J. Børve, J. J. Rehr, J. J. Kas, F. D. Vila, T. D. Thomas, and S. Svensson, "Nonstoichiometric Intensities in Core Photoelectron Spectroscopy," *Physical Review Letters*, vol. 108, no. 19, 2012.

[6] S. T. Manson and A. F. Starace, "Photoelectron Angular Distributions: Energy Dependence for S Subshells," *Review of Modern Physics*, vol. 54, no. 2, 1982.

[7] B. Whitaker, *Imaging in Molecular Dynamics, Technology and Applications*. Cambridge University Press, 2003.

[8] K. M. Kadish, K. M. Smith, and R. Guilard, *Applications of Phthalocyanines*, vol. 19. Academic Press, 2004.

[9] M. G. Walter, "Porphyrins and Phthalocyanines in Solar Photovoltaic Cells," *Journal of Porphyrins and Phthalocyanines*, vol. 14, 2010.

[10] L. Wang, H. Qin, W. Zhang, L. Zhang, and D. Yan, "High Reliability of Vanadyl-Phthalocyanine Thin-Film Transistors using Silicon Nitride Gate Insulator," *Thin Solid Films*, vol. 545, pp. 514–516, 2013.

[11] C. J. Liu, J. J. Shih, and Y. H. Ju, "Surface Morphology and Gas Sensing Characteristics of Nickel Phthalocyanine Thin Film," *Sensors and Actuators B*, vol. 99, pp. 344–349, 2004.

[12] B. H. Bransden and C. J. Joachain, *Physics of Atoms and Molecules*. Pearson Education Limited, Second ed., 2003.

[13] G. Hahner, "Near Edge X-ray Absorption Fine Structure Spectroscopy as a Tool to Probe Electronic and Structural Properties of Thin Organic Films and Liquids," *Chem. Soc. Rev.*, vol. 35, pp. 1244–1255, 2006.

[14] W. F. Chan, G. Cooper, and C. E. Brion, "Absolute Optical Oscillator Strengths for the Electronic Excitation of Atoms at High Resolution: Experimental Methods and Measurements for Helium," *Phys. Rev. A*, vol. 44, pp. 186–204, Jul 1991.

[15] D. Attwood, *Soft X-Rays and Extreme Ultraviolet Radiation: Principles and Applications*. Cambridge university press, 1999.

[16] H. Siegfried, *Auger and X-ray Photoelectron Spectroscopy in Materials Science [Elektronisk resurs]: A User-Orientated Guide*. Springer Berlin Heidelberg: Imprint: Springer, 2013.

[17] K. Gunnelin, *Soft X-Ray Emission Studies of the Electronic Structure of Molecules*. PhD thesis, Uppsala University, 1997.

[18] J. W. Cooper, "Photoelectron-Angular-Distribution Parameters for Rare-Gas Subshells," *Physical Review A*, vol. 47, no. 3, 1993.

[19] M. Jung, B. Krässig, D. S. Gemmell, E. P. Kanter, T. LeBrun, S. H. Southworth, and L. Young, "Experimental Determination of Nondipolar Angular Distribution Parameters for Photoionization in the Ar K and Kr L Shells," *Phys. Rev. A*, vol. 54, pp. 2127–2136, 1996.

[20] E. Månsson, *Ultra-fast Dynamics in Atoms and Molecules during Photoionization*. PhD thesis, Lund Univeristy, 2014.

[21] S.-C. Yang and R. Bersohn, "Theory of the Angular Distribution of Molecular Photofragments," *The Journal of Chemical Physics*, vol. 61, no. 11, pp. 4400–4407, 1974.

[22] V. Schmidt, "Photoionization of Atoms using Synchrotron Radiation," *Reports on Progress in Physics*, vol. 52, 1992.

[23] A. Sankari, *Relativistic Atomic Structure Calculations Applied to Electronic Transitions in Atoms*. Acdemic Dissertation, Univeristy of Oulu, 2008.

[24] R. G. Houlgate, J. B. West, K. Codling, and G. V. Marr, "The Angular Distribution of the 3_p Electrons and the Partial Cross Section of the 3_s Electrons of Argon from Threshold to 70 eV," *Journal of Electron Spectroscopy and Related Phenomena*, vol. 9, pp. 205–209, 1976.

[25] P. O'Keeffe, P. Bolognesi, R. Richter, A. Moise, Y. Ovcharenko, G. King, and L. Avaldi, "Velocity-Map Imaging of Near-Threshold Photoelectrons in Ne and Ar," *Physical review A*, vol. 84, 2011.

[26] C. Isvoranu, *Metal-Organic Complexes at Surfaces*. Phd thesis, Lund University, 2010.

[27] S. Hüfner, *Photoelectron Spectroscopy*. Springer-Verlag, 1995.

[28] K. Hagen, *Organic Electronics II: More Materials and Applications*. 2012.

[29] V. Schmidt, *Electron Spectrometry of Atoms using Synchrotron Radiation*. Cambridge University press, 1997.

[30] M. Nakamura, M. Sasanuma, S. Sato, M. Watanabe, H. Yamashita, Y. Iguchi, A. Ejiri, S. Nakai, S.and Yamaaguchi, T. Sagawa, Y. Nakai, and T. Oshio, "Absorption Structure Near the L $_{II,III}$ Edge of Argon Gas," *Physical Review Letters*, vol. 21, 1968.

[31] M. Bässler, A. Ausmees, M. Jurvansuu, R. Feifel, J.-O. Forsell, P. de Tarso Fonseca, A. Kivimäki, S. Sundin, S. Sorensen, R. Nyholm, O. Björneholm, S. Aksela, and S. Svensson, "Beam Line I411 at MAX II - Performance and First Results," *Nuclear Instruments and Methods in Physics Research Section A: Accelerators, Spectrometers, Detectors and Associated Equipment*, vol. 469, no. 3, pp. 382 – 393, 2001.

[32] L. Avaldi, G. Dawber, R. Camilloni, G. King, M. Roper, M. R. F. Siggel, G. Stefani, and M. Zitnik, "Near-Threshold Photoionization of the Ar 2p Subshell," *Journal of Physics B: Atomic, Molecular and Optical Physics*, vol. 27, no. 17, p. 3953, 1994.

[33] D. A. Chestakov, S. M. Wu, G. Wu, and D. H. Parker, "Slicing Using a Conventional Velocity Map Imaging Setup: O_2, I_2 and I_2^+ Photodissociation," *The Journal of Physical Chemistry A*, vol. 108, 2004.

[34] A. G. Suits and R. E. Continetti, *Imaging in Chemical Dynamics: The State of the Art*, ch. 1, pp. 1–18. No. 770 in ACS Symposium Series, Oxford University Press, 2000.

[35] A. B. Eppink and D. Parker, "Velocity Map Imaging of Ions and Electrons using Electrostatic Lenses: Application in Photoelectron and Photofragment Ion Imaging of Molecular Oxygen," *Rev. Sci. Instrum.*, vol. 68, no. 9, 1997.

[36] G. A. Garcia, L. Nahon, and I. Powis, "Two-dimensional Charged Particle Image Inversion Using a Polar Basis Function Expansion," *Review of Scientific Instruments*, vol. 75, no. 11, p. 4989, 2004.

[37] D. Chandler and P. Houston, "Two-Dimensional Imaging of State-Selected Photodissociation Products Detected by Multiphoton Ionization," *Journal of Chemical Physics*, vol. 87, no. 2, pp. 1445–1447, 1987.

[38] M. J. J. Vrakking, "An iterative Procedure for the Inversion of Two-Dimensional Ion/Photoelectron Imaging Experiments," *Review of Scientific Instruments*, vol. 72, 2001.

[39] D. Lindle, L. Medhurst, A. Ferrett, P. Heimann, M. Piancastelli, S. Liu, and D. Shirley, "Angle-resolved Photoemission from the Ar 2p Subshell," *Physical Review A*, vol. 38, no. 5, 1988.

[40] J. A. R. Samson, Y. Lu, and W. C. Stolte, "Aspects of Postcollision Interactions (PCI) Near the Ar L-Shell," *Physical Review A*, vol. 56, 1997.

[41] B. Paripas, G. Vitez, G. Viktor, K. Tokesi, A. Calo, R. Sankari, M. Huttula, S. Aksela, and H. Aksela, "Angular dependence of the PCI line shape for Photoionised Ne K-LL and Ar L-MM Auger transitions," *Journal of Physics B: Atomic, Molecular and Optical Physics*, vol. 37, 2004.

[42] M. Ehara, T. Horikawa, R. Fukuda, H. Nakatsuji, T. Tanaka, M. Kato, H. Hoshino, H. Tanaka, R. Feifel, and K. Ueda, "Symmetry and Vibrationally Resolved Absorption Spectra Near the N K Edges of N_2O: Experiment and Theory," *Physical Review A*, vol. 83, 2011.

[43] Y. Ma, C. T. Chen, G. Meigs, K. Randall, and F. Sette, "High resolution K-Shell Absorption Measurements of Simple Molecules," *Physical Review A*, vol. 44, 1991.

[44] J. D. Bozek, N. Saito, and I. H. Suzuki, "Asymmetry in the Ionic fragmentation of N_2O Photoexcited Around the N and O K Edges," *The Journal of Chemical Physics*, vol. 98, p. 4652, 1993.

[45] R. Lucchese, J. Söderström, T. Tanaka, M. Hoshino, M. Kitaima, H. Tanaka, A. De Fanis, J. E. Rubensson, and K. Ueda, "Vibrationally Resolved Partial Cross Sections and Asymmetry Parameters for Nitrogen K-shell Photoionition of the N2O Molecule," *Physical Review A*, vol. 76, no. 1, 2007.

[46] R. Guillemin, O. Hemmers, D. Lindle, and S. Manson, "Experimental Investigation of Nondipole Effects in Photoemission at the Advanced Light Source," *Radiation Physics and Chemistry*, vol. 75, pp. 2258–2274, 2006.

[47] H. K. Tseng, R. H. Pratt, S. Yu, and A. Ron, "Photoelectron Angular Distributions," *Phys. Rev. A*, vol. 17, pp. 1061–1079, 1978.

[48] O. Hemmers, R. Guillemin, and D. Lindle, "Non Dipole Effects in Soft X-ray Photoemission," *Radiation Physics and Chemistry*, vol. 70, pp. 123–47, 2004.

[49] M.-S. Liao and S. Scheiner, "Electronic Structure and Bonding in Metal Phthalocyanines, Metal = Fe, Co, Ni, Cu, Zn, Mg," *Journal of Chemical Physics*, vol. 114, 2001.

[50] T. Kroll, R. Kraus, R. Schönfelder, V. Y. Aristov, and O. Molodtsova, "Transition Metal Phthalocyanines: Insight into the Electronic Structure from Soft X-ray Spectroscopy," *The Journal of Chemical Physics*, vol. 137, 2012.

[51] M. Grobosch, C. Schmidt, R. Kraus, and M. Knupfer, "Electronic Properties of Transition metal Phthalocyanines: The Impact of the Central Metal Atom (d^5–d^{10})," *Organic Electronics*, vol. 11, pp. 1483–1488, 2010.

[52] L. Ottaviano, L. Lozzi, F. Ramondo, P. Picozzi, and S. Santucci, "Copper Hexadecafluoro Phthalocyanine and Naphthalocyanine: The Role of Shake up Excitations in the Interpretation and Electronic Distinction of High-resolution X-ray Photoelectron Spectroscopy Measurements,"

Journal of Electron Spectroscopy and Related Phenomena, vol. 105, pp. 145–154, 1999.

[53] O. Plekan, V. Feyer, R. Richter, M. Coreno, M. de Simone, and K. C. Prince, "Photofragmentation of Guanine, Cytosine, Leucine and Methionine," *Chemical Physics*, vol. 334, pp. 53–63, 2007.